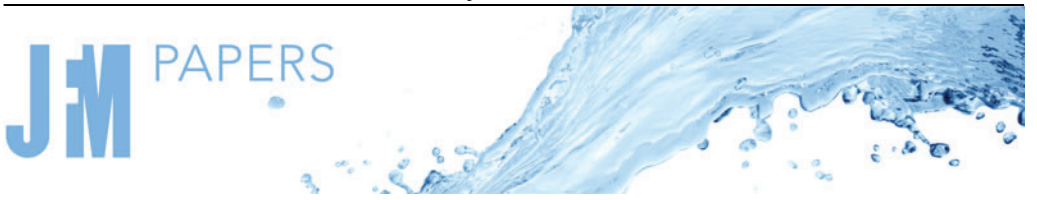
J. Fluid Mech. (2025), *vol*. 1005, A15, doi:10.1017/jfm.2024.1116



Absolute instability in the higher-generation airways: a pathway for airway closure

Ramkarn Patne†

Department of Chemical Engineering, Indian Institute of Technology Hyderabad, Kandi, Sangareddy, Telangana 502285, India

(Received 6 May 2024; revised 15 November 2024; accepted 18 November 2024)

Experiments on microfluidic core–annular flows demonstrated a transition from a continuous core jet to core-fluid drops and slugs separated by the annular fluid films/slugs due to absolute instability. The flows in the higher-generation airways could be modelled as core–annular flow with the laminar core airflow and annular airway surface liquid (ASL). Thus, if an absolute instability exists in the higher-generation airways, then it could lead to ASL film/slug-induced airway closure, necessitating the present study. Taking cues from previous studies, we derive an evolution equation using the lubrication approximation. The analysis, using the dispersion relation obtained from the evolution equation, predicts the existence of the critical capillary number Ca_c such that, for $Ca < Ca_c$, the flow will be absolutely unstable for vanishing Reynolds number Re. The parameter Ca_c exhibits the scaling as $Ca_c \sim (1-H)^2/\mu_r$, where $1-H$ is the dimensionless thickness of the ASL, and μ_r is the ratio of the air viscosity to the ASL viscosity. In agreement with the experimental observations, for a healthy lung, the analysis predicts absolute instability triggered airway closure only at the end of expiration during a breathing cycle. For a diseased lung, the ASL thickness and viscosity drastically increase the possibility of absolutely unstable flow and, thus, airway closure. Increasing inertial effect (i.e. Re) exacerbates airway closure by curtailing the convectively unstable region. Similarly, the ASL shear thinning widens the absolute instability parametric region. Thus, the present analysis demonstrates a pathway for airway closure in the higher-generation airways due to absolute instability.

Key words: pulmonary fluid mechanics, absolute/convective instability, core-annular flow

1. Introduction

The airways play an indispensable role in gas conduction and exchange in the human respiratory system. The trachea is considered zeroth-generation airway while primary bronchi connecting lungs to the trachea are considered first-generation airways (Pedley

† Email address for correspondence: ramkarn@che.iith.ac.in

© The Author(s), 2025. Published by Cambridge University Press

https://doi.org/10.1017/jfm.2024.1116 Published online by Cambridge University Press

1977). The lungs possess up to 23 generations of airways, with the terminal alveolar sacs as the last generation where gas exchange occurs (Jain & Sznajder 2007; Grotberg 2011). Airways with an inner diameter of less than 2 mm or beyond tenth generation are generally classified as the higher-generation or distal airways characterised by laminar airflow in contrast with the turbulent airflow in the lower-generation or proximal airways (Jain & Sznajder 2007; Lin *et al.* 2007). The inside of the airway walls is lined by airway surface liquid (ASL) consisting of two layers, *viz.*, the inner viscoelastic mucus layer and the outer Newtonian serous layer up to the 15th generation of the airways. Only a serous layer lines the walls of the later airways (Grotberg 2011). Thus, as airflow occurs during inspiration or expiration, there will be a core–annular flow with air occupying the core region and ASL occupying the annular region. The ASL may lead to the formation of liquid bridges or slugs and subsequent airway closure in the higher-generation airways due to the film collapse triggered by the Rayleigh–Plateau instability (Heil, Hazel & Smith 2008; Romano *et al.* 2019; Erken *et al.* 2021, 2023; Muradoglu *et al.* 2021).

Experiments by Guillot *et al.* (2007) and Utada *et al.* (2008) on microfluidic core–annular flows through a tube have demonstrated the existence of core-fluid drop or slug formation due to absolute instability. These core-fluid drops or slugs are separated by the annular fluid bridges or slugs, which can occlude the tube. Thus, the absolute instability could provide a pathway for airway closure. However, conclusions from the existing studies regarding absolute instability are not applicable to the core–annular flow in the higher-generation airways due to the extreme parametric range relevant to these airways, which remains unexplored in the previous analyses. For example, the viscosity ratio of the air to the ASL is $\sim 10^{-5} - 10^{-3}$ depending on the presence of pulmonary diseases (Lai *et al.* 2009; Hill *et al.* 2014; Lafforgue *et al.* 2017). Additionally, there is density stratification, extremely small thickness of the ASL (Widdicombe & Widdicombe 1995; Widdicombe 1997), appreciable inertial forces due to a considerable air velocity in earlier generations of the distal airways (Pedley 1977) and the viscoelastic nature of the ASL.

Thus, whether the core–annular flow in the higher-generation airways exhibits absolute instability remains unknown. This leads to a simple question: Is there an absolute instability in the higher-generation airways even in this extreme parametric regime? If there is an absolute instability, how does variation in the ASL thickness, elasticity and viscosity affect its existence? The present study makes an effort to answer these questions. To accomplish this, we model fluid flows in the higher-generation airways as a laminar core–annular flow through a tube with the air as the core fluid and viscoelastic ASL as the annular fluid. The model will be justified in the following discussion.

1.1. *Absolute/convective instability in core–annular flows*

A core–annular flow of two immiscible Newtonian flows can become unstable due to the Rayleigh–Plateau or capillary instability associated with the interfacial tension, henceforth termed the capillary mode (Utada *et al.* 2007, 2008; Guillot, Colin & Ajdari 2008). Also, if the viscosities of the fluids differ, then depending on the interface position, a new mode due to viscosity stratification could arise (Wei 2005*a*,*b*; Wei & Rumschitzki 2005; Gaurav & Shankar 2007; Govindarajan & Sahu 2014). This mode was first predicted for viscosity stratified plane channel flow by Yih (1967); thus, henceforth, we will refer to this mode as Yih mode. In the present study, the annular fluid is viscoelastic, while the core fluid is Newtonian. Thus, there is also elasticity stratification, leading to another mode of instability, henceforth termed the elastic mode (Chen 1991).

https://doi.org/10.1017/jfm.2024.1116 Published online by Cambridge University Press

The temporally unstable core–annular flow due to the three modes, *viz*., capillary, Yih and elastic modes, could lead to an absolutely unstable flow or convectively unstable flow depending on the value of the imaginary part of the complex frequency at the cusp point (Briggs 1964; Kupfer, Bers & Ram 1987). An absolutely unstable flow leads to the development of the temporally unstable mode in up- and down-stream directions while a convectively unstable flow signifies that the disturbances develop only in the downstream direction from the source of the disturbances (Briggs 1964).

The experimental and theoretical investigation of core–annular flows for the existence of absolute instability is due to Utada *et al.* (2007, 2008) and Guillot *et al.* (2007, 2008). Their experiments demonstrated the existence of a continuous core-fluid jet, core-fluid slugs and drops depending on the flow rate of the fluids. To understand the experimental observations, Guillot *et al.* (2007) derived a flow model using lubrication theory and showed that their experimental and theoretical results are in excellent agreement. Their theoretical model neglected inertial effects, considered Newtonian fluids and ignored the density stratification.

Salin & Talon (2019) analysed the transition from convective to absolute instability in a core–annular flow of two immiscible Newtonian fluids. Their analysis considered both viscosity and density stratification and investigated the effect of various parameters on the transition. Sahu (2021) reported a new type of interfacial mode associated with the axisymmetric and corkscrew perturbations for certain ranges of viscosity and density ratios in immiscible liquid–liquid core–annular flow. Note that Sahu (2021) did not investigate the existence of absolute instability. Dietze & Ruyer-Quil (2015) predicted occlusion due to nonlinear waves in narrow tubes. Dietze, Lavalle & Ruyer-Quil (2020) studied a gravity-driven liquid film falling down the inner surface of a narrow cylindrical tube in the presence of an active core-gas flow and predicted occlusion due to surface waves. Elaborate treatment of two-layer thin film flows, and application of the long-wave model is discussed at length in Dietze (2022). Note that the focus of Dietze & Ruyer-Quil (2015) and Dietze *et al.* (2020) is to understand the occlusion of a narrow tube due to the development of linear instabilities and spatially growing waves that lead to the occlusion. As mentioned by Dietze *et al.* (2020), the occlusion scenario explored in their analysis differs from those induced by absolute instability, although they have also reported parametric regimes where the absolute instability is relevant.

1.2. *Dynamics of flows in airways*

Several studies have investigated the linear and nonlinear dynamics of the stability of the ASL in rigid and compliant tubes (Grotberg & Jensen 2004; Heil *et al.* 2008; Grotberg 2011). Halpern & Grotberg (1992) investigated the stability of airway closure phenomena by modelling the ASL as a static liquid layer lining the inner surface of a compliant tube. Their analysis predicted a possibility of airway closure due to the capillary mode assisted by the tube compliance. Halpern & Grotberg (1993) extended the analysis of Halpern & Grotberg (1992) by including surfactant at the air–liquid interface. Their analysis predicted a delay in the airway closure due to the surfactant. Moriarty & Grotberg (1999) studied the stability of a two-layer flow to mimic the shearing flow of the mucus and serous layers by the airflow. White & Heil (2005) developed a thin-film model for airway closure due to the Rayleigh–Plateau instability. Halpern, Fujioka & Grotberg (2010) demonstrated the destabilising influence of the ASL viscoelasticity on the instabilities exhibited by a liquid flowing under the influence of gravity. Zhou *et al.* (2014) extended the analysis of Halpern *et al.* (2010) to include the effect of an insoluble surfactant and imposed shear at the free surface.

https://doi.org/10.1017/jfm.2024.1116 Published online by Cambridge University Press

Camassa, Ogrosky & Olander (2014) theoretically and experimentally analysed the evolution of a gravity-driven flow of a viscous liquid film coating the inside of a tube. The role of core turbulent airflow was considered through interfacial stresses created by the airflow. Their analysis predicted liquid plug formation for thicker films. Camassa, Ogrosky & Olander (2017) studied the stability of a liquid film driven against gravity by a constant volume flux of air through the centre of the tube. They derived a one-sided model by accounting for the turbulent stresses exerted by the flowing air.

Romano *et al.* (2019) analysed the liquid plug formation in the airways owing to the capillary instability. Romano *et al.* (2021) demonstrated the vital role of the elasticity of the mucus on the airway closure scenario. Erken *et al.* (2021) treated the mucus and serous layers as two layers, unlike in the previous studies where the ASL was treated as a single layer. Their analysis predicted closure in the two-layer model much sooner than that in the corresponding one-layer model. Romano, Muradoglu & Grotberg (2022) studied the effect of surfactant on the airway closure scenario. Patne (2021) analysed the effect of wall deformability and ASL elasticity on the sheared flow in the lower-generation airways. His analysis predicted the flow to be unconditionally unstable. Shemilt *et al.* (2022, 2023) and Erken *et al.* (2023) analysed the effect of the viscoplastic nature of the mucus on the airway closure scenarios. Recently, Patne (2024) predicted the stabilisation of the instabilities in the lower generation airways due to hot air inhalation and the opposite for cold air inhalation. An excellent review on the mechanism of airway closure by Heil *et al.* (2008) discusses the role of airway instabilities in causing airway closure.

Note that, besides film collapse, owing to the compliant nature of airway walls, the airways could undergo compliant collapse, wherein the airway's inner diameter could decrease due to wall compression (Halpern & Grotberg 1992, 1993; Heil *et al.* 2008). The decreased airway inner diameter then enhances the capillary instability to result in the closure of the airway. Here, we assume a rigid tube; thus, the present analysis focuses on the film collapse due to absolute instability.

1.3. *Present study*

Burger & Macklem (1968) experimentally demonstrated the airway closure in small airways with inner diameter $\sim$0.9 mm of healthy humans. Using the Weibel & Gomez (1962) formula $d = d_0\, 2^{-n/3}$, inner diameter $\sim$0.9 mm corresponds to 11th to 14th generation of the airways where d is the diameter of the nth generation of the airway and d_0 is the diameter of the trachea. Note that the inner diameter of the trachea is $\sim$1.5–2 cm (Pedley 1977; Grotberg 2011; Standring 2016). For the airways up to the 15th generation, the ASL consists of mucus and serous layers lining the airways (Grotberg 2011). Thus, we must use a viscoelastic model to describe the dynamics of the annular ASL. Due to pulmonary diseases, the ASL thickness can increase substantially, which could lead to airway closure even in earlier generations of the airways (Heil *et al.* 2008). Following previous studies (Heil *et al.* 2008; Romano *et al.* 2019, 2021; Patne 2021, 2024; Shemilt *et al.* 2022), we assume the ASL as a single viscoelastic liquid layer by considering average properties of the mucus and serous layers.

In the lower-generation airways, the airflow is turbulent owing to the large Reynolds number and laryngeal jet (Pedley 1977). As discussed in Patne (2024), instead of core–annular flow, a shear flow driven by turbulent stresses (due to turbulent airflow) exists in the lower-generation airway ASL. Thus, the flow dynamics is drastically different in the higher-generation airways, thereby necessitating the present study.

The ASL exhibits a strong shear-thinning viscoelastic behaviour. The previous experimental studies indicate that the ASL viscosity and relaxation time exhibit a

https://doi.org/10.1017/jfm.2024.1116 Published online by Cambridge University Press

power-law variation for an increasing shear rate with power-law index $n \sim 0.1$–05 (Lai *et al.* 2009). Thus, a fluid model which considers both the properties is necessary to successfully capture the dynamics of ASL. These requirements are fulfilled by the phenomenological White & Metzner (1963) (WM) model. The WM model introduces shear thinning by assuming dependence of the viscosity and relaxation time on the second invariant of the strain-rate tensor. Thus, data reported in the literature for the rheological parameters of the WM model can be readily fit into the power-law model, thereby making it easy to relate the experimental observations to theoretical predictions. Note that the WM model has been previously utilised by Wilson & Rallison (1999), Wilson & Loridan (2015), Castillo & Wilson (2017), Patne (2021) and Patne *et al.* (2024) to investigate the stability of rectilinear shear flows.

Owing to the large difference in the densities and viscosities of the air and the ASL, fluid layers with density and viscosity stratification must be considered. Considering these factors, to determine the existence of absolute instability in the higher-generation airways, we model the fluid flow as a core–annular flow of two immiscible fluids with a strong density, elasticity and viscosity stratification. The core fluid is Newtonian, while the annular fluid is a shear-thinning viscoelastic WM fluid. In the spirit of the lubrication-theory-based model of Guillot *et al.* (2007) and long-wave equation of Camassa *et al.* (2014), here, we derive an evolution equation for the flow using long-wave analysis. The obtained equation is then utilised to determine the dispersion relation and investigate the existence of absolute instability.

The rest of the paper is arranged as follows. In § 2, the base state, boundary conditions and perturbation governing equations are derived. The numerical methodology utilised here to solve the eigenvalue problem is presented in § 3. The general linear stability analysis, i.e. stability analysis at arbitrary wavenumber, and corresponding discussion, are presented in § 4. The analytical model based on the thin-film equation is formulated and discussed in § 5. The temporal and spatio-temporal stability analyses are discussed in §§ 6 and 7, respectively. Finally, the major conclusions obtained in the present study are summarised in § 8.

2. Problem formulation

Consider a core–annular flow of two immiscible fluids with an incompressible Newtonian fluid in the core region and an incompressible shear-thinning viscoelastic liquid layer in the annular region flowing through a tube of radius R. The core fluid possesses a constant dynamic viscosity μ_1^*, density ρ_1 and occupies region $r^* \in [0, HR]$, where $0 \leq H \leq 1$. Here, the superscript '$*$' signifies a dimensional quantity, which will be scaled in the following discussion. The ASL has shear-rate-dependent dynamic viscosity μ_2^* and relaxation time λ_2^*, constant shear modulus G, density ρ_2 and occupies region $r^* \in [HR, R]$. The schematic of the flow under consideration is shown in figure 1 in terms of the lengths scaled by the radius of the tube.

To include the shear-thinning nature of the ASL, the dimensional ASL viscosity (μ_2^*) and relaxation time (λ^*) are assumed to be functions of the second invariant ($\dot{\gamma}^*$) of the strain-rate tensor $\dot{\boldsymbol{\gamma}}^{*(2)} = (\boldsymbol{\nabla} \boldsymbol{v}^{*(2)}) + (\boldsymbol{\nabla} \boldsymbol{v}^{*(2)})^{\mathrm{T}}$. Following earlier studies (Wilson, Renardy & Renardy 1999; Patne 2021), we employ power-law model

$$\mu_2^*(\dot{\gamma}^*) = K \dot{\gamma}^{*(n-1)}, \tag{2.1}$$

https://doi.org/10.1017/jfm.2024.1116 Published online by Cambridge University Press

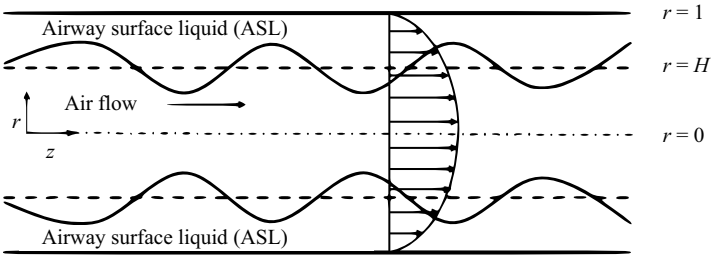


Figure 1. Schematic of the model core–annular flow geometry in dimensionless coordinates. Waves at the air–ASL interface signify the development of interfacial instability.

$$\lambda_2^*(\dot{\gamma}^*) = \frac{\mu_2^*(\dot{\gamma}*)}{G_f} = \frac{K}{G}\dot{\gamma}^{*(n-1)}, \tag{2.2}$$

$$\dot{\gamma}^* = \sqrt{\tfrac{1}{2}\dot{\gamma}_{ij}^{*(2)}\dot{\gamma}_{ji}^{*(2)}}. \tag{2.3}$$

Here, K is the consistency parameter in the power-law model and n is the power-law index.

The velocities and lengths are scaled by V_c and R, respectively, where V_c is the velocity of the core fluid at the centre of the airway. The viscosity and relaxation time are scaled by viscosity scale $\mu_s = K(V_c/R)^{(n-1)}$ and μ_s/G, respectively. The pressure ($p^{(i)}$) and stress components ($\boldsymbol{\tau}^{(i)}$) are non-dimensionalised by $\mu_s V_c/R$. Thus, the scaled ASL viscosity and relaxation time are

$$\mu_2(\dot{\gamma}) = \lambda(\dot{\gamma}) = \dot{\gamma}^{(n-1)}. \tag{2.4a}$$

Let $\boldsymbol{v}^{(i)} = (v_r^{(i)}, v_\theta^{(i)}, v_z^{(i)})$ be the dimensionless velocity fields in fluid where $i = 1$ for the core fluid and $i = 2$ for the annular fluid. The scaled continuity and Cauchy momentum equations are

$$\boldsymbol{\nabla} \cdot \boldsymbol{v}^{(i)} = 0, \tag{2.4b}$$

$$\rho^{(i)}\, Re\left[\frac{\partial \boldsymbol{v}^{(i)}}{\partial t} + (\boldsymbol{v}^{(i)} \cdot \boldsymbol{\nabla})\boldsymbol{v}^{(i)}\right] = -\boldsymbol{\nabla} p^{(i)} + \boldsymbol{\nabla} \cdot \boldsymbol{\tau}^{(i)}, \tag{2.4c}$$

where $Re = \rho_2 V_c R/\mu_s$ is the Reynolds number and $\boldsymbol{\nabla}$ is the gradient operator. The parameter $\rho^{(i)}$ is $\rho^{(1)} = \rho_r$ for the core fluid and $\rho^{(2)} = 1$ for the annular fluid. The core fluid is a Newtonian fluid; thus we assume $\boldsymbol{\tau}^{(1)} = \mu_r \dot{\boldsymbol{\gamma}}^{(1)}$, where $\mu_r = \mu_1/\mu_s$ and $\dot{\boldsymbol{\gamma}}^{(1)} = (\boldsymbol{\nabla}\boldsymbol{v}^{(1)}) + (\boldsymbol{\nabla}\boldsymbol{v}^{(1)})^{\mathrm{T}}$ is the strain-rate tensor. For the annular viscoelastic fluid, we employ the WM model (Wilson & Rallison 1999; Patne 2021)

$$\boldsymbol{\tau}^{(2)} + W\lambda(\dot{\gamma})\left[\frac{\partial \boldsymbol{\tau}^{(2)}}{\partial t} + \boldsymbol{v}^{(2)} \cdot \boldsymbol{\tau}^{(2)} - (\boldsymbol{\nabla}\boldsymbol{v}^{(2)})^{\mathrm{T}} \cdot \boldsymbol{\tau}^{(2)} - \boldsymbol{\tau}^{(2)} \cdot (\boldsymbol{\nabla}\boldsymbol{v}^{(2)})\right] = \mu_2(\dot{\gamma})\dot{\boldsymbol{\gamma}}^{(2)}, \tag{2.4d}$$

where $W = \mu_s V_c/(GR)$ is the Weissenberg number.

At the air–ASL interface ($r = H$), the above equations are supplemented with the kinematic boundary condition, velocity continuity and tangential and normal stress balance conditions. No-slip and impermeability conditions are applied at $r = 1$, i.e. at the ASL–airway muscle interface.

Note that the oscillatory airflow due to breathing and the branching network of the bifurcating airways will certainly modify the predictions of the present study.

https://doi.org/10.1017/jfm.2024.1116 Published online by Cambridge University Press

These factors have been neglected in the flow considered here in order to simplify the extremely complicated flows in the airways and make the flow amenable to theoretical treatment. Considering an oscillatory airflow necessitates linear Floquet stability analysis, which becomes a cumbersome mathematical exercise when applied to investigate the spatio-temporal stability analysis. The present study aims to provide a theoretical basis for the experimental observations using, admittedly, a simplified model by focusing on a single airway.

For a laminar flow of a Newtonian fluid, the length of the pipe (L) necessary to achieve a fully developed flow is (White 2003; Incropera *et al.* 2007)

$$L \approx 0.06 Re_D D, \tag{2.5a}$$

where $Re_D = \rho U D/\mu$ is the Reynolds number based on the diameter D of the pipe and uniform inlet velocity U. For the higher-generation airways, $Re_D \sim O(10^{-3} - 10)$ implies that a fully developed flow exists in the airways for $L > 0.6D$. In the Stokes flow ($Re_D \to 0$) limit, the development length is comparable to the airway diameter, implying the existence of a fully developed flow for $L > D$ (Badr *et al.* 1985; Stocker & Duck 1995; Abrahams, Davis & Smith 2008). The airway length is typically six times larger than its radius in higher airway generations (Crystal 1997). Thus, assuming that the above calculations apply to the flow under consideration, a fully developed flow exists for the most part of the airways for the range of Re_D considered here. For a steady-state, axisymmetric, fully developed base state, the quantities are

$$\bar{v}_z^{(1)} = \frac{(r^2 - H^2)}{4\mu_r}\frac{\partial \bar{p}}{\partial z} + \frac{n}{2^{1/n}(1+n)}\left[\left(-\frac{\partial \bar{p}}{\partial z}\right)^{1/n} - H\left(-H\frac{\partial \bar{p}}{\partial z}\right)^{1/n}\right], \tag{2.5b}$$

$$\bar{v}_z^{(2)} = \frac{n}{2^{1/n}(1+n)}\left[\left(-\frac{\partial \bar{p}}{\partial z}\right)^{1/n} - r\left(-r\frac{\partial \bar{p}}{\partial z}\right)^{1/n}\right], \tag{2.5c}$$

$$\frac{\partial \bar{p}}{\partial z} = -\frac{4\mu_r}{\mu_r + H^2(1-\mu_r)}, \tag{2.5d}$$

$$\bar{\tau}_{rz}^{(2)} = \bar{\mu}_2(\bar{\dot{\gamma}})\frac{\mathrm{d}\bar{v}_z^{(2)}}{\mathrm{d}r}; \quad \bar{\tau}_{zz}^{(2)} = 2W\bar{\lambda}(\bar{\dot{\gamma}})\bar{\tau}_{rz}^{(2)}\frac{\mathrm{d}\bar{v}_z^{(2)}}{\mathrm{d}r}, \tag{2.5e}$$

where an overbar signifies a base-state quantity and $\bar{\mu}_2(\bar{\dot{\gamma}}) = \bar{\lambda}(\bar{\dot{\gamma}}) = (-\mathrm{d}\bar{v}_z^{(2)}/\mathrm{d}r)^{(n-1)}$.

2.1. *Linearised perturbation equations*

We impose infinitesimal perturbations on the base state (2.5) and substitute in the governing equations (2.4). The resulting equations are then linearised around the base state (2.5) to obtain the linearised perturbation equations. Following Guillot *et al.* (2007) and Camassa *et al.* (2014), here, we consider axisymmetric perturbations. In the linearised perturbation equations, we substitute

$$\mathcal{F}'(\boldsymbol{x}, t) = \tilde{\mathcal{F}}(r)\,\mathrm{e}^{\mathrm{i}(kz - \omega t)}, \tag{2.6}$$

where $\mathcal{F}'(\boldsymbol{x}, t)$ and $\tilde{\mathcal{F}}(r)$ are the perturbation to a quantity and the corresponding eigenfunction, respectively. Here, $k = k_r + \mathrm{i}k_i$ is the wavenumber, and $\omega = \omega_r + \mathrm{i}\omega_i$ is the complex frequency of the perturbations. The base state (2.5) is temporally unstable if at least one eigenvalue satisfies the condition $\omega_i > 0$ for $k_i = 0$. For the flow to be absolutely unstable, the requirement will be explained in § 7.

https://doi.org/10.1017/jfm.2024.1116 Published online by Cambridge University Press

After substituting (2.6) in the linearised governing equations, we obtain

$$D\tilde{v}_r^{(i)} + \frac{\tilde{v}_r^{(i)}}{r} + \mathrm{i}k\tilde{v}_z^{(i)} = 0, \tag{2.7a}$$

$$\rho^{(i)}\, Re[\mathrm{i}\tilde{v}_z^{(i)}(k\bar{v}_z^{(i)} - \omega) + D\bar{v}_z^{(i)}\tilde{v}_r^{(i)}] = -\mathrm{i}k\tilde{p}^{(i)} + \mathrm{i}k\tilde{\tau}_{zz}^{(i)} + D\tilde{\tau}_{rz}^{(i)} + \frac{1}{r}\tilde{\tau}_{rz}^{(i)}, \tag{2.7b}$$

$$\mathrm{i}\rho^{(i)}\, Re\, \tilde{v}_r^{(i)}(k\bar{v}_z^{(i)} - \omega) = -D\tilde{p}^{(i)} + \mathrm{i}k\tilde{\tau}_{rz}^{(i)} + D\tilde{\tau}_{rr}^{(i)} + \frac{1}{r}(\tilde{\tau}_{rz}^{(i)} - \tilde{\tau}_{\theta\theta}^{(i)}), \tag{2.7c}$$

where $D = \mathrm{d}/\mathrm{d}r$. For the core fluid, the stress tensor components are

$$\tilde{\tau}_{zz}^{(1)} = 2\mathrm{i}k\mu_r\tilde{v}_z^{(1)}; \quad \tilde{\tau}_{rz}^{(1)} = \mu_r(D\tilde{v}_z^{(1)} + \mathrm{i}k\tilde{v}_r^{(1)}), \tag{2.7d}$$

$$\tilde{\tau}_{rr}^{(1)} = 2\mu_r D\tilde{v}_r^{(1)}; \quad \tilde{\tau}_{\theta\theta}^{(1)} = \frac{2\mu_r}{r}\tilde{v}_r^{(1)}. \tag{2.7e}$$

The constitutive equation (2.4*d*) gives

$$\begin{aligned} &W\bar{\lambda}(\bar{\dot{\gamma}})[(\mathrm{i}k\bar{v}_z^{(2)} - \omega)\tilde{\tau}_{zz}^{(2)} + \tilde{v}_r^{(2)}D\bar{\tau}_{zz}^{(2)} - 2\mathrm{i}k\bar{\tau}_{zz}^{(2)}\tilde{v}_z^{(2)} - 2D\bar{v}_z^{(2)}\tilde{\tau}_{rz}^{(2)} - 2\bar{\tau}_{rz}^{(2)}D\tilde{v}_z^{(2)}] \\ &- 2W\bar{\tau}_{rz}^{(2)}D\bar{v}_z^{(2)}\left(\frac{\mathrm{d}\lambda}{\mathrm{d}\dot{\gamma}}\right)_{\dot{\gamma}=\bar{\dot{\gamma}}}[\mathrm{i}k\tilde{v}_r^{(2)} + D\tilde{v}_z^{(2)}] + \tilde{\tau}_{zz}^{(2)} = 2\mathrm{i}k\bar{\mu}_2(\bar{\dot{\gamma}})\tilde{v}_z^{(2)}, \end{aligned} \tag{2.7f}$$

$$\begin{aligned} &W\bar{\lambda}(\bar{\dot{\gamma}})[\mathrm{i}k(\bar{v}_z^{(2)} - c)\tilde{\tau}_{rz}^{(2)} + \tilde{v}_r^{(2)}D\bar{\tau}_{rz}^{(2)} - \mathrm{i}k\bar{\tau}_{rz}^{(2)}\tilde{v}_z^{(2)} - D\bar{v}_z^{(2)}\tilde{\tau}_{rr}^{(2)} - \mathrm{i}k\bar{\tau}_{zz}^{(2)}\tilde{v}_r^{(2)} - \bar{\tau}_{rz}^{(2)}D\tilde{v}_r^{(2)}] \\ &+ \tilde{\tau}_{rz}^{(2)} = n(\mathrm{i}k\tilde{v}_r^{(2)} + D\tilde{v}_z^{(2)}), \end{aligned} \tag{2.7g}$$

$$W\bar{\lambda}(\bar{\dot{\gamma}})[\mathrm{i}k(\bar{v}_z^{(2)} - c)\tilde{\tau}_{rr}^{(2)} - 2\mathrm{i}k\bar{\tau}_{rz}^{(2)}\tilde{v}_r^{(2)}] + \tilde{\tau}_{rr}^{(2)} = 2\bar{\mu}_2(\bar{\dot{\gamma}})D\tilde{v}_r^{(2)}, \tag{2.7h}$$

$$W\bar{\lambda}(\bar{\dot{\gamma}})[\mathrm{i}k(\bar{v}_z^{(2)} - c)\tilde{\tau}_{\theta\theta}^{(2)}] + \tilde{\tau}_{\theta\theta}^{(2)} = 2\bar{\mu}_2(\bar{\dot{\gamma}})\frac{\tilde{v}_r^{(2)}}{r}. \tag{2.7i}$$

To solve the above (2.7), we utilise the following boundary conditions. At the centre of the tube, for the axisymmetric disturbances

$$u^{(1)} = 0 \quad \text{and} \quad \partial_r v^{(1)} = 0. \tag{2.8a}$$

At the air–ASL interface, let the interface be specified by $r = H + h(z, t)$. Here, $h(z, t)$ is the imposed perturbation on the interface. At $r = H$, the relevant boundary conditions include the kinematic boundary condition and the continuity of the velocity and stress components (Wei 2005*a*; Wei & Rumschitzki 2005; Bassom, Blyth & Papageorgiou 2012; Gaurav & Shankar 2013)

$$\mathrm{i}(k\bar{v}_z^{(1)} - \omega)\tilde{h} = \tilde{v}_r^{(1)}, \tag{2.8b}$$

$$\tilde{v}_r^{(1)} = \tilde{v}_r^{(2)}, \tag{2.8c}$$

$$\tilde{v}_z^{(1)} + D\bar{v}_z^{(1)}\tilde{h} = \tilde{v}_z^{(2)} + D\bar{v}_z^{(2)}\tilde{h}, \tag{2.8d}$$

$$\tilde{\tau}_{rz}^{(1)} = -2\mathrm{i}kW(D\bar{v}_z^{(2)})^2\tilde{h} + \tilde{\tau}_{rz}^{(2)}, \tag{2.8e}$$

$$-\tilde{p}^{(1)} + \tilde{\tau}_{rr}^{(1)} + \tilde{p}^{(2)} - \tilde{\tau}_{rr}^{(2)} = \frac{1}{Ca}\left(\frac{1}{H^2} - k^2\right)\tilde{h}, \tag{2.8f}$$

where $h(z, t) = \tilde{h}\,\mathrm{e}^{\mathrm{i}(kz-\omega t)}$ and $Ca = \mu_s V_c/\Sigma_0^*$ is the capillary number. At $r = 1$, i.e. at the ASL–muscle interface, we assume no slip and impermeability of the airway wall

$$\tilde{v}_r = 0, \quad \tilde{v}_z = 0. \tag{2.8g}$$

https://doi.org/10.1017/jfm.2024.1116 Published online by Cambridge University Press

Dimensionless parameter	Order of magnitude
W	$10^{-2} - 10^{2}$
Ca	$10^{-3} - 10^{2}$
Re	$10^{-3} - 10^{2}$
μ_r	$10^{-4} - 10^{-2}$
ρ_r	10^{-3}
n	0.1–0.5

Table 1. Order of magnitude of the dimensionless parameters using the dimensional parameters listed in the text. Note that the viscosity and density of the air are $\sim 10^{-5}$ Pa·s and ~ 1 kg m^{-3}.

The present study aims to understand the ASL layer dynamics in the higher-generation airways. Thus, first, we estimate the relevant parameters. In these airways, the thickness of the ASL layer in a healthy lung is $\sim O(10^{-6} - 10^{-7})$ m while the airway lumen radius is $\sim O(10^{-3} - 10^{-4})$ m; thus $H \sim 1$ (Widdicombe & Widdicombe 1995; Widdicombe 1997; Moriarty & Grotberg 1999; Montaudon *et al.* 2007; Furlow & Mathisen 2018; Karamaoun *et al.* 2018). The respiratory diseases could substantially increase the thickness of the ASL layer, thus H could assume values much less than unity (Shah *et al.* 1996; Moriarty & Grotberg 1999; Heil *et al.* 2008). The power-law index (n) for the ASL is 0.1–0.5 (Lai *et al.* 2009).

The density and viscosity of the ASL and air–ASL interfacial tension are $\sim 10^{3}$ kg m^{-3}, $\sim 10^{-1} - 10^{-2}$ N m^{-1} and $\sim 10^{2} - 10^{-2}$ Pa·s, respectively (Hwang, Litt & Forsman 1969; Li, Xu & Kumacheva 2000; Schatz & Neitzel 2001; Lai *et al.* 2009; Hamed & Fiegel 2014; Hill *et al.* 2014; Chen *et al.* 2019). The maximum velocity of air in the higher-generation airways is $V_c \sim 10^{-3} - 1$ m s^{-1} (Pedley 1977). The velocity decreases as the air travels to the higher generation of airways. This leads to a laminar airflow in the higher-generation airways (Lin *et al.* 2007; Kleinstreuer & Zhang 2009, 2010; Xia *et al.* 2010). The order of magnitude of the dimensionless parameters is given in table 1.

3. Numerical methodology

To solve the eigenvalue problem (2.7) subjected to the boundary conditions (2.8), we employ the pseudo-spectral method. Each eigenfunctions are expanded in terms of the Chebyshev polynomials

$$\tilde{f}(y) = \sum_{m=0}^{m=M} a_m \mathcal{T}_m(y), \tag{3.1}$$

where $\mathcal{T}_m(y)$ are Chebyshev polynomials of degree m and M is the highest degree of the polynomial in the series expansion or, equivalently, the number of collocation points. The series coefficients a_m are the unknowns to be solved for. The generalised eigenvalue problem is constructed in the form

$$\boldsymbol{Ae} + \omega \boldsymbol{Be} = 0, \tag{3.2}$$

where $\boldsymbol{A}$ and $\boldsymbol{B}$ are the discretised matrices and $\boldsymbol{e}$ is the vector of a_m.

The standard procedure for the discretisation procedure of the matrices can be found in Trefethen (2000) and Schmid & Henningson (2001). To solve the so-formed eigenvalue problem, we employ the eig MATLAB routine. Along with the genuine eigenvalues, the pseudo-spectral code also predicts numerically spurious eigenvalues. To filter out these

https://doi.org/10.1017/jfm.2024.1116 Published online by Cambridge University Press

spurious eigenvalues, we compare the numerically computed spectrum for N and $N+2$ collocation points with *a priori* specified tolerance, e.g. 10^{-6}. The genuine eigenvalues are further verified by increasing the number of collocation points by 25 and monitoring the variation of the obtained eigenvalues. Whenever the eigenvalue does not change up to a prescribed precision, e.g. to the fifth significant digit, the same number of collocation points is used to determine the critical parameters of the system. The above-described numerical methodology has been previously utilised to solve similar problems by Patne (2021, 2024), Patne & Shankar (2020) and Patne & Chandarana (2023). To validate the numerical methodology described above, the results predicted by the numerical method will be compared with the analytically obtained solution in § 6.

4. General linear stability analysis

From previous studies of Chen (1991), Hu & Patankar (1995), Gaurav & Shankar (2013), Wei (2005*a*,*b*), Bassom *et al.* (2012), Joseph *et al.* (1997) and Wei & Rumschitzki (2005), the present flow geometry can exhibit the Yih mode due to viscosity stratification, the elastic mode due to the viscoelastic nature of the ASL and the capillary mode due to the interfacial tension. The existence of these modes is demonstrated in figure 2. From the analysis of Yih (1967), the Yih or viscosity stratification mode exhibits a non-zero growth rate for a finite Re, which can be positive depending on the viscosity ratio and interface position. From figure 2(*a*) for $\mu_r < 1$ and $H > 0.8$, the growth rate is positive. The existence of the capillary mode is demonstrated in figure 2(*b*). In agreement with the previous studies (Hu & Patankar 1995; Joseph *et al.* 1997; Wei 2005*a*,*b*; Wei & Rumschitzki 2005; Bassom *et al.* 2012; Gaurav & Shankar 2013), the capillary mode exhibits an increasing growth rate for a decreasing capillary number. The elastic mode shown in figure 2(*c*) arises due to the first normal stress difference across the air–ASL interface (Chen 1991). From figure 2, the three instability modes relevant to the present study are long wave. Thus, we proceed with deriving the evolution equation to carry out the stability of the flow.

5. Evolution equation

To derive the long-wave evolution equation describing the dynamics of the liquid layers for the disturbances, let λ be the wavelength of the long-wave disturbances such that $R = \epsilon\lambda$, where $\epsilon \ll 1$. Now, following the procedure described in Oron, Davis & Bankoff (1997), Samanta (2013), Patne, Agnon & Oron (2021) and Patne & Chandarana (2023), we scale the z-axis and time as: $z \to Z\epsilon^{-1}$ and $t \to \tau\epsilon^{-1}$. While the fluid dynamical quantities are expanded as

$$v_z^{(i)} = u_0^{(i)} + \epsilon u_1^{(i)} + \cdots, \tag{5.1a}$$

$$v_r^{(i)} = \epsilon v_0^{(i)} + \epsilon^2 v_1^{(i)} + \cdots, \tag{5.1b}$$

$$p^{(i)} = \frac{1}{\epsilon}\Pi_0^{(i)} + \Pi_1^{(i)} + \cdots. \tag{5.1c}$$

The elastic mode arises due to the first normal stress difference across the fluid–fluid interface, while the other elastic terms in the linearised constitutive equations (2.7*f*)–(2.7*i*) involving W provide a negligible quantitative correction, as shown in the table 2 in the absence of shear thinning. Due to this, we have neglected elastic terms in the linearised

https://doi.org/10.1017/jfm.2024.1116 Published online by Cambridge University Press

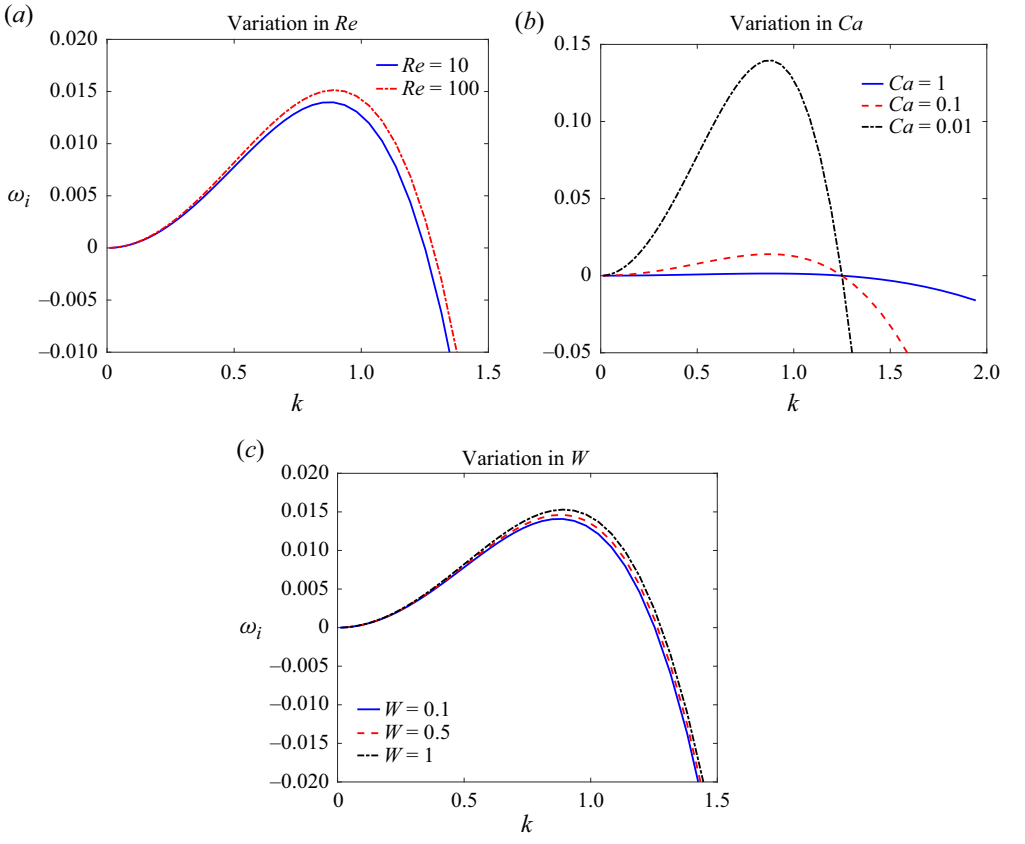


Figure 2. Variation in the growth rate ω_i with the disturbance wavenumber k at $\mu_r = 0.1$, $H = 0.8$, $n = 1$ and $\rho_r = 0.001$. Note that $\omega_i > 0$ implies an unstable mode. Panel (*a*) shows the destabilising effect of an increasing Reynolds number Re for $W = 0$ and $Ca = 0.1$, thereby demonstrating the existence of the Yih mode. Panel (*b*) demonstrates the capillary mode for $W = 0$ and $Re = 0$. Panel (*c*) demonstrates the elastic mode for $Re = 0$ and $Ca = 0.1$. A finite value of Ca is considered in panels (*a*) and (*c*) to remove the unphysical arbitrarily high wavenumber instability.

Parameters	Eigenvalue with elastic Terms in (2.7*f*)–(2.7*i*)	Eigenvalue without elastic Terms in (2.7*f*)–(2.7*i*)
$k = 0.1$	$8.77492 \times 10^{-5} + 4.16437 \times 10^{-4}i$	$8.77481 \times 10^{-5} + 4.16443 \times 10^{-4}i$
$k = 0.5$	$0.000436989 + 0.00865014i$	$0.000436973 + 0.00865002i$
$k = 1.5$	$0.00127306 - 0.0356675i$	$0.00127287 - 0.0356695i$

Table 2. The most unstable (least stable) numerically computed eigenvalue with/without elastic terms in the linearised constitutive equations (2.7*f*)–(2.7*i*) for $Re = 0$, $H = 0.8$, $W = 10$, $\mu_r = 0.001$, $n = 1$ and $Ca = 0.1$. A comparison of the last two columns indicates the negligible role of the elastic terms in the linearised constitutive equations (2.7*f*)–(2.7*i*).

constitutive equations (2.7*f*)–(2.7*i*). Thus, we incorporate the elastic effect only through the air–ASL interface tangential stress boundary condition. This assumption considerably simplifies the analysis while retaining the elastic characteristic of the ASL. Note that the analysis demonstrated here is restricted to $n = 1$ for the ASL since, for $n \neq 1$, the expressions become unwieldy to show here. For $O(\epsilon)$ calculations, MATHEMATICA fails

https://doi.org/10.1017/jfm.2024.1116 Published online by Cambridge University Press

to solve the equations for $n \neq 1$ due to an extremely high number of terms. Thus, the effect of the shear thinning on the inertial terms will not be shown here.

At the leading order $O(\epsilon^0)$, after substitution of the expansions (5.1) into the governing equations, (2.4) reduce to

$$-\partial_Z \Pi_0^{(i)} + \frac{\mu^{(i)}}{r}\partial_r(r\partial_r u_0^{(i)}) = 0, \quad \partial_r \Pi_0^{(i)} = 0. \tag{5.2a,b}$$

Equations (5.2) are subjected to the following boundary conditions. At the centre of the tube ($r = 0$) and tube wall ($r = 1$), the boundary conditions are

$$\text{at } r = 0, \quad u_0^{(1)} \text{ is finite and } \partial_r v_0^{(1)} = 0, \tag{5.3a}$$

$$\text{at } r = 1, \quad u_0^{(2)} = 0 \text{ and } v_0^{(2)} = 0. \tag{5.3b}$$

At the fluid–fluid interface $y = \zeta(z, t)$, the continuity of the velocity continuity and stress balance gives

$$u_0^{(1)} = u_0^{(2)}, \tag{5.3c}$$

$$v_0^{(1)} = v_0^{(2)}, \tag{5.3d}$$

$$\mu_r \partial_r u_0^{(1)} - \partial_r u_0^{(2)} = -2\hat{W}_m \partial_Z \zeta, \tag{5.3e}$$

$$\Pi_0^{(1)} - \Pi_0^{(2)} = -\widehat{Ca}^{-1}\left(\frac{\zeta}{H^2} + \partial_Z^2 \zeta\right), \tag{5.3f}$$

where

$$\hat{W}_m = \epsilon W (D\bar{v}_z^{(2)})^2 \quad \text{and} \quad \widehat{Ca} = \epsilon^{-3} Ca, \tag{5.3g}$$

are the scaled Weissenberg and capillary numbers, respectively.

The solution of the governing equations (5.2) using boundary conditions (5.3) leads to

$$u_0^{(1)} = a_1 + a_2 \ln r + \frac{1}{2\mu_r}\partial_Z \Pi_0^{(1)}, \tag{5.4a}$$

$$u_0^{(2)} = a_3 + a_4 \ln r + \frac{1}{2}\partial_Z \Pi_0^{(2)}, \tag{5.4b}$$

where a_i are the integration constants

$$a_1 = \frac{a_1'}{4Ca\,H^2(-\mu_r + (-1+\mu_r)\zeta^4)}, \tag{5.4c}$$

$$a_1' = -16Ca\,H^2\mu_r q - 8\zeta\, Ca\,H^2\mu_r \hat{W}_m(1 + \ln\zeta)\partial_Z\zeta$$
$$+ 8\zeta^3\, Ca\,H^2(-1+2\mu_r)\hat{W}_m\partial_Z\zeta + 8\zeta^5\, Ca\,H^2(-1+\mu_r)\hat{W}_m(-1+\ln\zeta)\partial_Z\zeta$$

https://doi.org/10.1017/jfm.2024.1116 Published online by Cambridge University Press

$$+(-3+4\mu_r)\zeta^4(\partial_Z\zeta+H^2\partial_Z^3\zeta)+2(-1+\mu_r)(-1+\ln\zeta)\zeta^6(\partial_Z\zeta+H^2\partial_Z^3\zeta)$$
$$+(1-2\mu_r-2\mu_r\ln\zeta)\zeta^2\partial_Z\zeta+H^2\zeta^2(16Ca\,(-1+\mu_r)q+(1-2\mu_r-2\mu_r\ln\zeta)\partial_Z^3\zeta, \tag{5.4d}$$

$$a_2=0, \tag{5.4e}$$

$$a_3=\frac{\partial_Z\zeta}{4Ca\,H^2}+\frac{\partial_Z^3\zeta}{4Ca}+\frac{\mu_r H^2(-16Ca\,q+(-1+\zeta^2)^2\partial_Z^3\zeta)}{4Ca\,H^2(-\mu_r+(-1+\mu_r)\zeta^4)}$$
$$+\frac{\mu_r[(-1+\zeta^2)(-1+8Ca\,H^2\hat{W}_m\zeta+\zeta^2)\partial_Z\zeta]}{4Ca\,H^2(-\mu_r+(-1+\mu_r)\zeta^4)}, \tag{5.4f}$$

$$a_4=\frac{\zeta^2}{2Ca\,H^2}(\partial_Z\zeta+H^2\partial_Z^3\zeta)+2\hat{W}_m\zeta\,\partial_Z\zeta, \tag{5.4g}$$

where q is the volumetric flow rate obtained using the base-state velocity profiles (2.5).

The rescaled kinematic boundary condition at the interface up to $O(1)$ is

$$\partial_\tau\zeta=-\frac{1}{\zeta}\partial_Z\int_0^\zeta r u_0^{(1)}\,\mathrm{d}r. \tag{5.5}$$

On substitution of the velocity profiles derived above into (5.5), the interface evolution equation can be obtained

$$\mathcal{F}_1(\zeta,\partial_Z\zeta,\partial_Z^2\zeta,\partial_Z^3\zeta,\partial_Z^4\zeta)+\mathcal{F}_2(\zeta)\partial_t\zeta=0, \tag{5.6}$$

where $\mathcal{F}_1(\zeta,\partial_Z\zeta,\partial_Z^2\zeta,\partial_Z^3\zeta,\partial_Z^4\zeta)$ and $\mathcal{F}_2(\zeta)$ are known functions.

To include the effect of the inertia, we proceed with $O(\epsilon)$ calculations. Adding the inertial effects leads to a better agreement between the long-wave model and numerically computed eigenvalues. At $O(\epsilon)$ the governing equations lead to

$$\rho_r Re(\partial_\tau u_0^{(i)}+u_0^{(i)}\partial_Z u_0^{(i)}+v_0^{(i)}\partial_r u_0^{(i)})=-\partial_Z\Pi_1^{(i)}+\frac{\mu^{(i)}}{r}\partial_r(r\partial_r u_1^{(i)}), \tag{5.7a}$$

$$\partial_r\Pi_1^{(i)}=0. \tag{5.7b}$$

The radial velocity $v_0^{(i)}$ can be derived using $u_0^{(i)}$ by using the continuity equation at $O(1)$. The boundary conditions at $O(\epsilon)$ are

$$\text{at } r=0,\quad u_1^{(1)} \text{ is finite and } \partial_r v_1^{(1)}=0, \tag{5.8a}$$

$$\text{at } r=1,\quad u_1^{(2)}=0 \text{ and } v_1^{(2)}=0. \tag{5.8b}$$

At the fluid–fluid interface, the interface conditions are

$$u_1^{(1)}=u_1^{(2)}, \tag{5.8c}$$

$$v_1^{(1)}=v_1^{(2)}, \tag{5.8d}$$

$$\mu_r\partial_r u_1^{(1)}-\partial_r u_1^{(2)}=0, \tag{5.8e}$$

$$\Pi_1^{(1)}-\Pi_1^{(2)}=0. \tag{5.8f}$$

The system of (5.7) is solved using the boundary conditions (5.8) to obtain the $O(\epsilon)$ contribution. At $O(\epsilon)$, equations turn out to be quite large; thus, we do not provide explicit

https://doi.org/10.1017/jfm.2024.1116 Published online by Cambridge University Press

expressions for the quantities. The rescaled kinematic boundary condition at the interface up to $O(\epsilon)$ is

$$\partial_\tau \zeta = -\frac{1}{\zeta}\partial_Z \int_0^\zeta r(u_0^{(1)} + \epsilon u_1^{(1)})\,\mathrm{d}r. \tag{5.9}$$

Using the above kinematic boundary condition, we obtain the evolution equation for the thickness of the layers. Before proceeding further, we scale out the ϵ parameter by rescaling the obtained equation. Thus, the parameters used below will be without hat subscript. The subsequent temporal and spatio-temporal stability analysis will be performed using the rescaled evolution equation.

6. Temporal stability analysis

As mentioned previously, due to the extreme density and viscosity stratification and the small thickness of the ASL in the higher-generation airways, the results from the previous studies dealing with the core–annular flow will not be readily relevant. Thus, first, we determine the relevance of the three modes of instability discussed in § 4 as follows. We linearise the evolution equation by substituting $\zeta = H + \zeta'$, where $\zeta' \ll 1$. Next, we use normal modes $\zeta' = \tilde{\zeta}\,\mathrm{e}^{\mathrm{i}(kz-\omega t)}$ in the resulting linearised equation to obtain the dispersion relation

$$\omega = kf_0(H, \mu_r, n) + \mathrm{i}k^2\left[f_1(H, \mu_r, \rho_r, n)\,Re + f_2(H, \mu_r, n)W + \frac{f_3(H, \mu_r, n)}{Ca}\right] - \mathrm{i}H^2k^4\frac{f_3(H, \mu_r, n)}{Ca}. \tag{6.1}$$

Here, the volumetric flow rate q has been eliminated by using relation $q = \int_0^H \bar{v}_z^{(1)} r\,\mathrm{d}r + \int_H^1 \bar{v}_z^{(2)} r\,\mathrm{d}r$. The functions f_i are

$$f_0 = \frac{(H^2-1)\mu_r}{H^4(\mu_r-1)-\mu_r}, \quad f_1 = \frac{-H^4(\mu_r-1)g_1}{g_2}, \quad f_2 = \frac{2H^4\mu_r^2 g_3}{g_4}, \tag{6.2a}$$

$$f_3 = \frac{H}{16}\left[\frac{g_5}{H^4(\mu_r-1)-\mu_r} - 4\ln H\right], \tag{6.2b}$$

and

$$\begin{aligned} g_1 = -(H^2-1)\{&\mu_r^2(2\mu_r^2 - H^{12}(\mu_r-1)(-13+22\mu_r) \\ &+ H^2\mu_r(-9+56\mu_r) + H^{10}(\mu_r-1)(-83+152\mu_r) + \cdots \\ &H^4(-24+(217-314\mu_r)\mu_r) + \cdots \\ &H^8(-193+612\mu_r-434\mu_r^2) + 5H^6(27+4\mu_r(-31+28\mu_r))) + \cdots \\ &3H^2(H^8(-3+7H^2) + H^4(5-29H^2+59H^4-35H^6)\mu_r + \cdots \\ &2H^2(H^2-1)^2(6-33H^2+35H^4)\mu_r^2 - \cdots \\ &6(H^2-1)^4(11H^2-1)\mu_r^3 + 24(H^2-1)^5\mu_r^4)\rho_r\} \end{aligned}$$

https://doi.org/10.1017/jfm.2024.1116 Published online by Cambridge University Press

$$+ 24H^2[H^4(\mu_r - 1) - \mu_r]\{3\mu_r^3(\rho_r - 1)\cdots$$
$$+ 6H^2\mu_r^2(-1 + 2\mu_r + \rho_r - 2\mu_r\rho_r) - \cdots$$
$$6H^6(\mu_r - 1)\mu_r(-\mu_r - \rho_r + 2\mu_r\rho_r) + \cdots$$
$$H^8(\mu_r - 1)(\rho_r + \mu_r(-\mu_r + 3(\mu_r - 1)\rho_r)) + \cdots$$
$$2H^4\mu_r(\rho_r + \mu_r(6 - 7\mu_r + 9(\mu_r - 1)\rho_r))\}\ln H, \tag{6.2c}$$

$$g_2 = 144[H^4(\mu_r - 1) - \mu_r]^3[-H^2(\mu_r - 1) + \mu_r]^2, \tag{6.2d}$$
$$g_3 = -H^2 + H^4 - 2(H^2 - 1)^2\mu_r + 2(H^4(\mu_r - 1) - \mu_r)\ln H, \tag{6.2e}$$
$$g_4 = [H^4(\mu_r - 1) - \mu_r][-H^2(\mu_r - 1) + \mu_r]^2, \tag{6.2f}$$
$$g_5 = (H^2 - 1)[1 - 4\mu_r + H^2(4\mu_r - 3)]. \tag{6.2g}$$

The function $f_0(H, \mu_r, n)$ is the wave speed of the perturbations. The functions $f_0(H, \mu_r, n), f_1(H, \mu_r, \rho_r, n)$ and $f_3(H, \mu_r, n)$ are in agreement with the long-wave asymptotic analysis of Gaurav & Shankar (2013) for $\rho_r = 1$, thereby validating the present analysis.

For $n \neq 1$, the functions $f_0(H, \mu_r, n), f_2(H, \mu_r, \rho_r, n)$ and $f_3(H, \mu_r, n)$ are

$$f_0 = \frac{2^{-2-1/n}(H^2 - 1)}{\mu_r - H^4\mu_r + H^4 n}g_0'; \quad f_2 = \frac{2^{-2-1/n}H^{3+1/n}g_3'}{g_4'}, \tag{6.3a}$$
$$f_3 = -\frac{H}{16n}\left[\frac{g_5'}{\mu_r - H^4\mu_r + H^4 n} + 4\ln H\right], \tag{6.3b}$$

where

$$g_0' = -2^{1+1/n}\mu_r H(H^2 - 1)\left(-H\frac{\partial\bar{p}}{\partial z}\right)^{1/n}\frac{\partial\bar{p}}{\partial z}[H^2 + \mu_r + H^4(-1 - \mu_r + n)], \tag{6.3c}$$

$$g_3' = \left(-\frac{\partial\bar{p}}{\partial z}\right)^{1/n+1}[(H^2 - 1)(2(H^2 - 1)\mu_r - H^2 n) + 2(\mu_r - H^4\mu_r + H^4 n)\ln H], \tag{6.3d}$$

$$g_4' = n(\mu_r - H^4\mu_r + H^4 n), \tag{6.3e}$$
$$g_5' = (H^2 - 1)[n - 4\mu_r + H^2(4\mu_r - 3n)], \tag{6.3f}$$
$$\frac{\partial\bar{p}}{\partial z} = -\frac{4\mu_r}{\mu_r + H^2(1 - \mu_r)}. \tag{6.3g}$$

The above equations reduce to (6) for $n = 1$. As stated above, owing to computational difficulty, the effect of shear thinning on the inertial term will not be explored. An examination of terms in (6.1) provides valuable insight into three modes of instability as follows. The first term, $f_1(H, \mu_r, \rho_r, n)Re$, is clearly a function of the density and viscosity stratification and leads to the Yih mode. The second term, $f_2(H, \mu_r, n)W$, arises due to the first normal stress difference across the air–ASL interface. Interestingly, this term is also a function of the viscosity stratification, as indicated by the presence of μ_r in $f_2(H, \mu_r, n)$. The elastic instability mode predicted by Chen (1991) for the core–annular flow of

https://doi.org/10.1017/jfm.2024.1116 Published online by Cambridge University Press

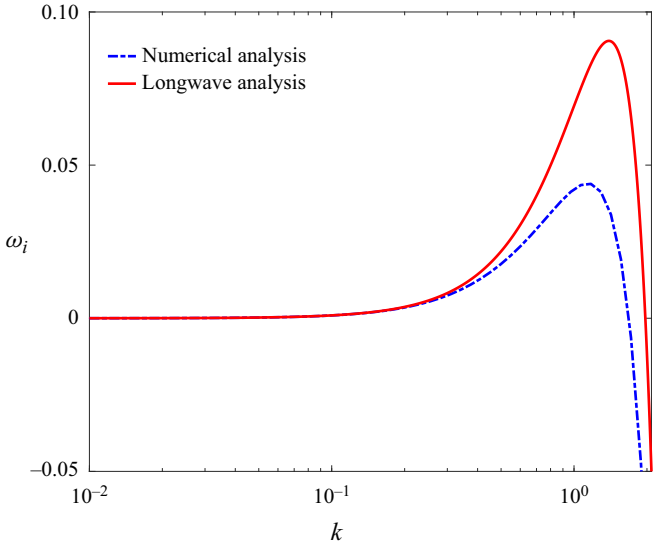


Figure 3. The variation of the growth rate (ω_i) with the wavenumber (k) for $Re = 10$, $W = 10$, $Ca = 0.1$, $n = 1$, $\mu_r = 0.1$, $H = 0.8$ and $\rho_r = 1$. The figure demonstrates excellent agreement between the numerical and asymptotic analyses for $k < 0.2$, thereby demonstrating the ability of the long-wave analysis. The semilog axis scale is used to magnify the low wavenumber region of the dispersion curve.

viscoelastic fluids is due to $f_2(H, \mu_r, n)W$. The third term, $f_3(H, \mu_r, n)/Ca$, arises due to the air–ASL interfacial tension and is responsible for the capillary mode. Additionally, all three functions depend on the power-law index, underlining the importance of the ASL shear thinning on the instabilities.

To demonstrate the utility of the evolution equation, we compare the growth rate predicted by the numerical and long-wave analyses in figure 3. Excellent agreement between the results predicted by both approaches for $k < 0.2$ certifies the applicability of the evolution equation. Since the analytical results have been validated by directly comparing the functions with Gaurav & Shankar (2013), figure 3 also validates the present numerical methodology.

The variation of $f_1(H, \mu_r, \rho_r, n)$ with H, ρ_r and μ_r is shown in figure 4. For the Yih mode to be unstable $f_1(H, \mu_r, \rho_r, n) > 0$, since $Re > 0$ in the present analysis. For $\mu_r < 1$, for low values of H, $f_1(H, \mu_r, \rho_r, n) < 0$ and the opposite case for high H, as shown in figure 4(a) in the absence of the density stratification, thus demonstrating the existence of the stable and unstable zones. From figure 4(b), the opposite scenario regarding $f_1(H, \mu_r, \rho_r, n)$ values is predicted for $\mu_r > 1$.

For the present problem, the inner fluid layer is air while the outer layer is ASL, thus $\rho_r \sim 10^{-3}$. From figure 4(c), $f_1(H, \mu_r, \rho_r, n) > 0$ for the whole range of H, implying the removal of the stable zone due to the density stratification. Depending on the diseases, the viscosity of the ASL also varies, and H could differ substantially from unity (Moriarty & Grotberg 1999; Hamed & Fiegel 2014). Thus, for these relevant parameters, $f_1(H, \mu_r, \rho_r, n)$ values are shown in figure 4(d), where $f_1(H, \mu_r, \rho_r, n) > 0$ irrespective of parametric combination. This implies that the Yih mode will lead to an unstable flow in the higher-generation airways.

The variation of $f_2(H, \mu_r, n)$ and $f_3(H, \mu_r, n)$ with H and μ_r is shown in figure 5. Note that $f_2(H, \mu_r, n)$ is the coefficient of W, thus representing elastic mode, while $f_3(H, \mu_r, n)$ is the coefficient of $1/Ca$, thus representing capillary mode. Similar to $f_1(H, \mu_r, \rho_r, n)$,

https://doi.org/10.1017/jfm.2024.1116 Published online by Cambridge University Press

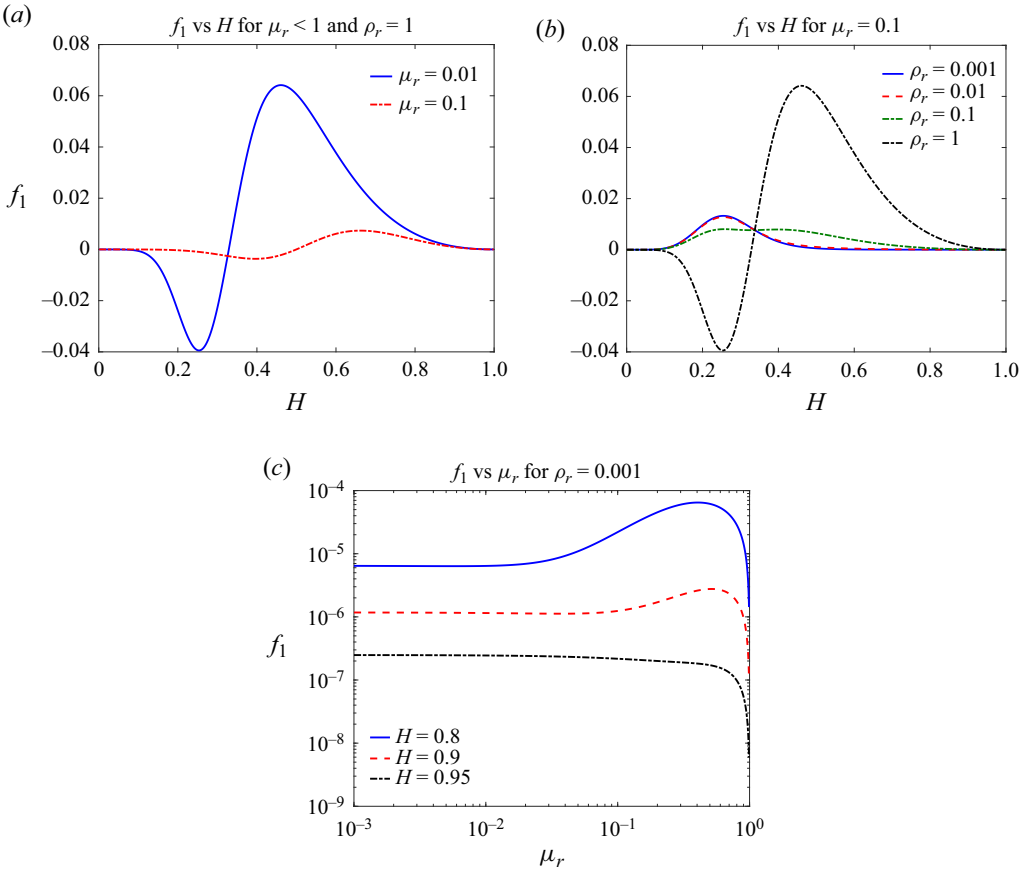


Figure 4. Variation of function $f_1(H, \mu_r, \rho_r, n)$ with the relative position of the liquid–liquid interface H and the viscosity ratio μ_r for $n = 1$. Note that $f_1(H, \mu_r, \rho_r, n) > 0$ implies an unstable Yih mode. Panels (*a*) and (*b*) show the presence of stable and unstable zones for $\mu_r < 1$ and $\mu_r > 1$, respectively. Panel (*c*) demonstrates the effect of variation in ρ_r on stable and unstable zones. Note the absence of stable zones for low ρ_r. Panel (*d*) shows the $f_1(H, \mu_r, \rho_r, n)$ values for the relevant parameters for the core–annular flow in the higher-generation airways.

$f_2(H, \mu_r, n)$ also exhibits negative values for low H, as shown in figure 5(*a*). The elastic and capillary modes are unstable if $f_2(H, \mu_r, n) > 0$ and $f_3(H, \mu_r, n) > 0$, respectively. For the parameters relevant to the higher-generation airways, from figure 5(*b*) $f_2(H, \mu_r, n) > 0$, implying the destabilising role of the ASL elasticity in the base flow. From figure 5(*c*), the capillary mode is unstable for an arbitrary value of H. The value of $f_3(H, \mu_r, n)$ for the parameters relevant to the core–annular flow in the higher-generation airways is shown in figure 5(*d*). To conclude from figures 4 and 5, the viscosity and density stratification, ASL elasticity and capillarity lead to the destabilisation of the core–annular flow in the higher-generation airways.

The effect of shear thinning on the elastic mode is shown in figure 6(*a*). For $\mu_r < 0.4$, an increasingly shear-thinning annular fluid has a strong stabilising effect on the elastic mode and the opposite for $\mu_r > 0.4$. For the capillary mode, as the shear-thinning index decreases and the viscosity of the ASL increases, the value of the function $f_3(H, \mu_r, n)$ increases, indicating a destabilising effect. This aspect is shown in figure 6(*b*) for select values of the power-law index n.

https://doi.org/10.1017/jfm.2024.1116 Published online by Cambridge University Press

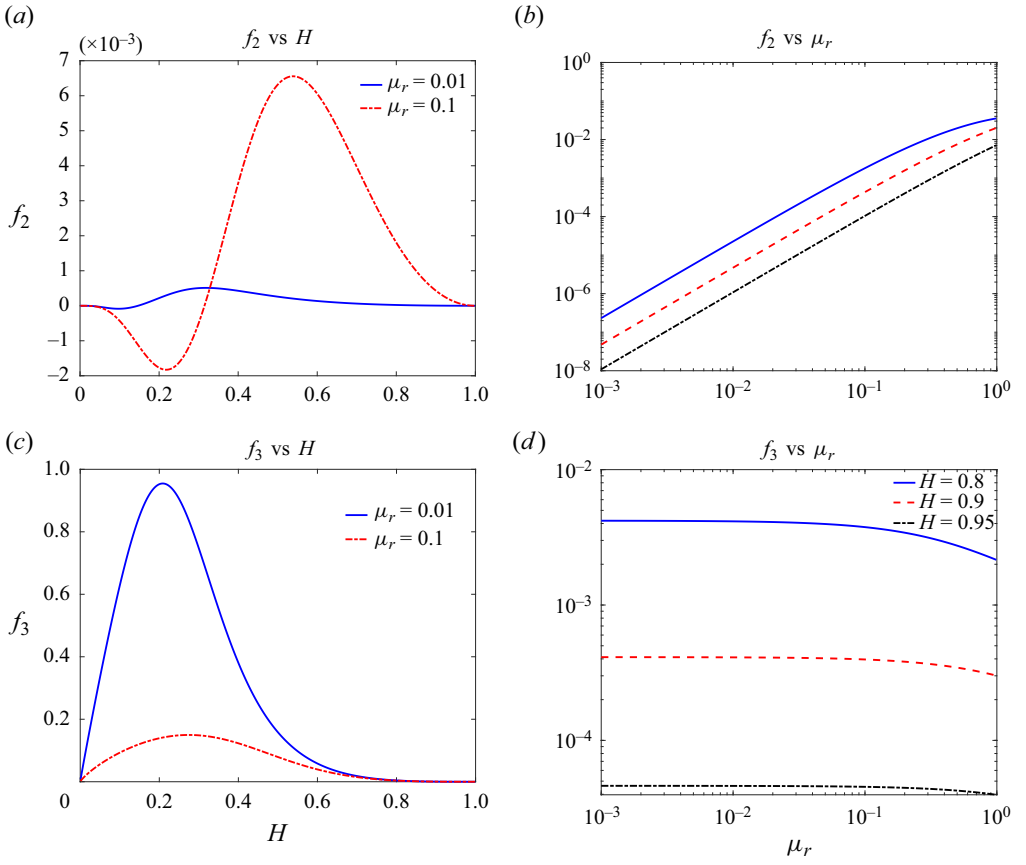


Figure 5. Variation of functions $f_2(H, \mu_r, n)$ and $f_3(H, \mu_r, n)$ with the relative position of the liquid–liquid interface H and the viscosity ratio μ_r for $n = 1$. Panel (*a*) demonstrates the existence of the stable and unstable zones for the elastic mode similar to $f_1(H, \mu_r, \rho_r, n)$. Panel (*c*) shows the existence of only an unstable zone for the capillary mode. Panels (*b*) and (*d*) show the values of the functions $f_2(H, \mu_r, n)$ and $f_3(H, \mu_r, n)$ relevant to the higher-generation airways.

7. Spatio-temporal stability analysis ($k_i \neq 0$)

In §§ 4 and 6, we assumed a complex frequency and real wavenumber, implying a temporal linear stability analysis. The flow is temporally unstable if the imaginary part of the frequency, $\omega_i > 0$, for at least one eigenvalue. Thus, temporal stability analysis provides information only about the temporal growth of the perturbations. Similarly, one can assume real frequency and complex wavenumber to carry out the spatial stability analysis. The flow will be spatially unstable if the imaginary part of the wavenumber, $k_i < 0$, for at least one eigenvalue. Thus, spatial stability provides information about the spatial growth of the perturbations. To analyse the growth of the perturbations in space and time, we must treat both frequency and wavenumber as complex numbers. The temporal and spatial stability analyses are straightforward and can be readily deduced from the eigenspectra. To analyse the spatio-temporal stability analysis, one can utilise methods developed by Briggs (1964) and Kupfer *et al.* (1987).

The spatio-temporal stability analysis classifies temporal instability as an absolute or convective instability depending on the value of ω_i at the cusp point. An absolutely unstable mode implies the development of the corresponding mode in up- and

https://doi.org/10.1017/jfm.2024.1116 Published online by Cambridge University Press

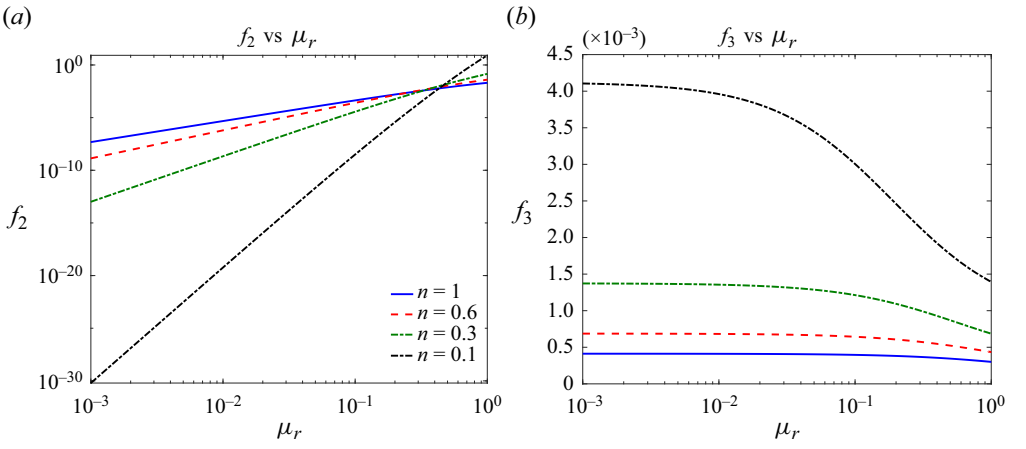


Figure 6. Variation of functions $f_2(H, \mu_r, n)$ (*a*) and $f_3(H, \mu_r, n)$ (*b*) with the relative viscosity μ_r for select values of power-law index n at $H = 0.9$. The figure demonstrates the stabilising effect of the shear-thinning nature of the ASL on the elastic mode and the opposite on the capillary mode.

down-stream directions while a convectively unstable mode signifies that the disturbances develop only in the downstream direction from the source of the disturbances (Briggs 1964). To demonstrate the absolute and convective instabilities, we assume an arbitrary dispersion relation $\omega = \mathcal{F}(k)$, where $\mathcal{F}(k)$ is a continuous and differentiable function of k. Next, we differentiate the dispersion relation with respect to k to obtain the group velocity of the perturbations. To determine the existence of absolute or convective instability, the group velocity of the disturbances is equated to zero so that $\partial\omega/\partial k = 0$ (Huerre & Monkewitz 1990; Schmid & Henningson 2001). The solution of this equation gives k values at which saddle points exist (denoted by k_0) in the k or $k_r - k_i$ plane. The calculated saddle point must also obey the causality principle for the existence of the absolute instability (Huerre & Monkewitz 1990). For the first-order saddle point in the k-plane, a local Taylor series expansion about this point gives $(\omega - \omega_0) \sim (k - k_0)^2$, where ω_0 is the cusp point in the ω or $\omega_r - \omega_i$ plane. This relationship implies that the mapping from the k-plane to the ω-plane is characterised by angle doubling (i.e. phase doubling). The solution of the equation $\partial\omega/\partial k = 0$ could lead to multiple solutions in terms of k. Among these solutions, if at least one saddle point satisfies the condition $\omega_{0i} > 0$, then the flow is absolutely unstable else convectively unstable (Kupfer *et al.* 1987; Huerre & Monkewitz 1990).

Briggs (1964) devised a method to determine the saddle point in the k-plane and the cusp point in the ω-plane by using analytic continuation. This method requires systematic movement of the curves in both planes from the temporal stability curves. This necessitates a considerable computation, which could become unwieldy for realistic flows. Kupfer *et al.* (1987) suggested an alternative method in which only the cusp point formation in the ω-plane is accomplished by varying k_i value. If, for a finite k_i, the cusp point in the ω-plane possesses $\omega_{i0} > 0$ and follows causality, then the flow is absolutely unstable. Given the relative ease of the Kupfer *et al.* (1987) method, it will be utilised in the present study.

The Kupfer *et al.* (1987) procedure to determine the genuine cusp point is as follows. We begin with the temporal curve in the ω-plane. This curve corresponds to $k_i = 0$ and varying k_r. Next, a finite negative value is assumed for k_i, and k_r varies similarly to the temporal curve. The same procedure is repeated until a cusp point forms in the ω-plane. To

https://doi.org/10.1017/jfm.2024.1116 Published online by Cambridge University Press

determine whether the obtained cusp point follows causality, a straight line parallel to the ω_i axis is drawn from the cusp point until it crosses the temporal curve. If the line crosses the temporal curve an odd number of times, then the obtained cusp point follows causality and is termed a genuine cusp point. Otherwise, it is an evanescent cusp point (Yeo, Khoo & Zhao 1999, 2001; Patne & Shankar 2017; Patne & Ramon 2020; Patne & Chandarana 2023).

To obtain the saddle point, we differentiate the dispersion relation (6.1) with respect to k and solve the resulting equation for k to obtain three roots

$$k_0 = -\frac{\mathrm{i}F_1}{3^{1/3}\Delta} + \frac{\mathrm{i}\Delta}{2\,3^{2/3}F_2}, \tag{7.1a}$$

$$k_0 = \frac{(\mathrm{i}-\sqrt{3})F_1}{2\,3^{1/3}\Delta} - \frac{(\mathrm{i}+\sqrt{3})\Delta}{4\,3^{2/3}F_2}, \tag{7.1b}$$

$$k_0 = \frac{(\mathrm{i}+\sqrt{3})F_1}{2\,3^{1/3}\Delta} - \frac{(\mathrm{i}-\sqrt{3})\Delta}{4\,3^{2/3}F_2}, \tag{7.1c}$$

where

$$\Delta = \left(9f_0F_2^2 + \sqrt{3}\sqrt{8F_1^3F_2^3 + 27f_0^2F_2^4}\right)^{1/3}, \tag{7.1d}$$

$$F_1 = f_1(H,\mu_r,\rho_r,n)Re + f_2(H,\mu_r,n)W + \frac{f_3(H,\mu_r,n)}{Ca} + f_4(H,\mu_r)Ma, \tag{7.1e}$$

$$F_2 = H^2\frac{f_3(H,\mu_r,n)}{Ca}. \tag{7.1f}$$

The first root (7.1*a*) is purely imaginary since the factors F_1, F_2 and Δ, are real numbers, thus a spurious saddle point. The second root (7.1*b*) will be a complex number with a negative real part. The third root (7.1*c*) is also a complex number but with a positive real part. In § 4, we considered positive real values of k while analysing the temporal stability analysis. Thus, the third root (7.1*c*) possessing a positive real part is the relevant root. Note that the second root (7.1*b*) will provide the same cusp point, albeit for negative values of k_r. Thus, the conclusions obtained using the third root (7.1*c*) will be applicable to the second root (7.1*b*) as well. To obtain the cusp point ω_0, the third root (7.1*c*) is substituted into the dispersion relation (6.1). Next, we investigate the effect of capillarity, inertia, ASL elasticity and viscosity in introducing an absolute instability.

7.1. *Effect of capillarity (Ca)*

The cusp points for select values of Ca and parameters relevant to the higher generation airways are shown in figure 7. Note that we will neglect the effect of inertia and ASL elasticity in this section to focus on the capillary effect. The cusp points are shown here to demonstrate the genuine nature of the cusp point as follows. To determine the genuine cusp point, a straight line is drawn from the cusp point parallel to the ω_i axis. From figure 7, for the values of Ca considered here, the line crosses the temporal curve only once, i.e. an odd number of times. From the above discussion, this implies the cusp points shown in figure 7 are genuine.

The role of capillary instability in causing absolute instability has been previously demonstrated by Guillot *et al.* (2007, 2008) and Utada *et al.* (2007). This does not imply an absolutely unstable flow for an arbitrary value of Ca, as shown in figure 7. For low

https://doi.org/10.1017/jfm.2024.1116 Published online by Cambridge University Press

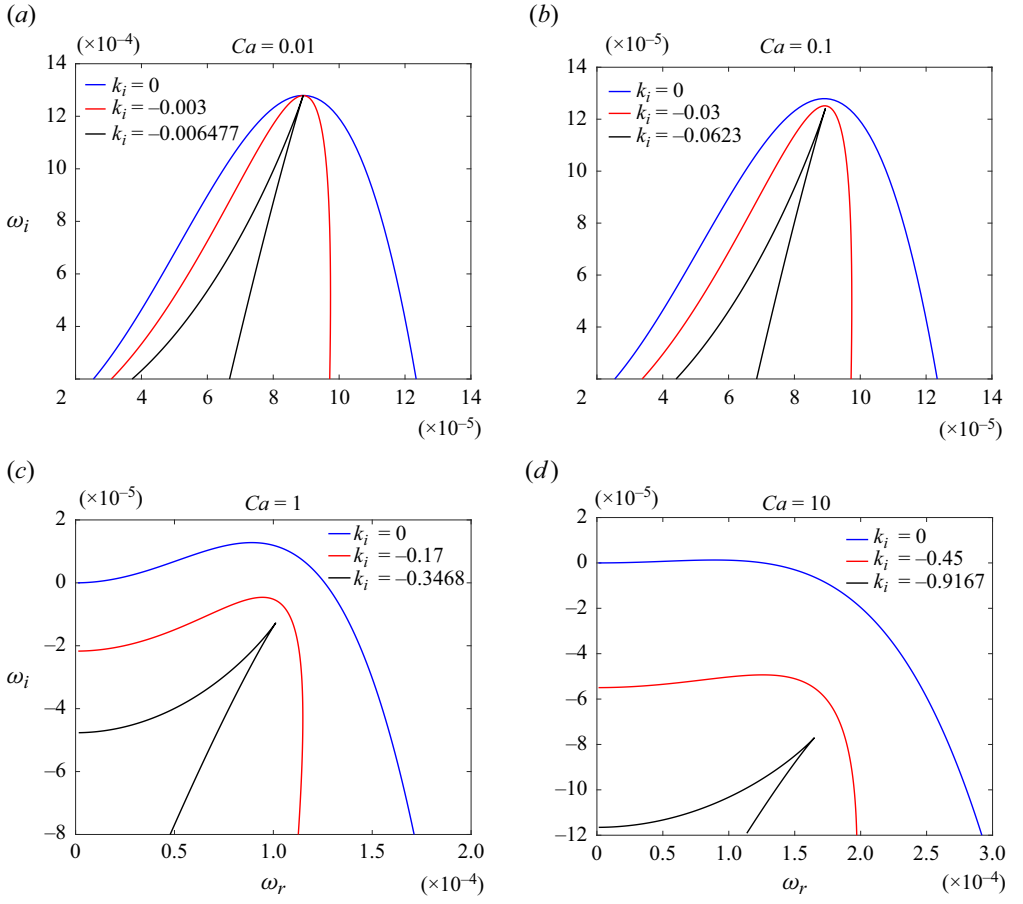


Figure 7. Cusp point formation in the ω-plane at $\mu_r = 0.001$, $H = 0.95$, $Re = 0$, $n = 1$ and $W = 0$. The locations of the saddle and cusp points in the k and ω planes for all panels are as follows: (*a*) $k_0 = 0.7444 - 0.006477i$, $\omega_0 = 0.00008908 + 0.001279i$; (*b*) $k_0 = 0.7523 - 0.06299i$, $\omega_0 = 0.00008940 + 0.0001241i$; (*c*) $k_0 = 0.9565 - 0.3468i$, $\omega_0 = 0.0001012 - 0.00001278i$; (*d*) $k_0 = 1.754 - 0.9167i$, $\omega_0 = 0.0001648 - 0.00007712i$. Note that, from dispersion relation (6.1), the flow is temporally unstable for a finite value of Ca.

Ca, the flow is absolutely unstable and convectively unstable for large values of Ca. Thus, there exists a critical value of the capillary number (Ca_c) for given values of H and μ_r beyond which the flow is convectively unstable. For the parameters specified in figure 7, $Ca_c = 0.6585$. From the definition of Ca, this implies a minimum ASL viscosity and/or core velocity is necessary to avoid absolute instability. Drawing an analogy with the experiments of Guillot *et al.* (2007) and Utada *et al.* (2007), the absolute instability predicted here could lead to the formation of air bubbles and ASL plugs in the airways. These ASL plugs could function similarly to the ASL bridges or plugs formed due to film collapse to result in airway closure. Thus, the information about the Ca_c could be utilised to predict the airway closure triggered by the absolute instability. Pulmonary diseases lead to an increase in the viscosity and thickness of the ASL (Hwang *et al.* 1969; Shah *et al.* 1996; Lai *et al.* 2009; Chen *et al.* 2019). In the core–annular flow under consideration, the dimensionless thickness of the ASL layer is $1 - H$. Thus, we determine the variation of Ca_c with $1 - H$ and μ_r in figure 8.

https://doi.org/10.1017/jfm.2024.1116 Published online by Cambridge University Press

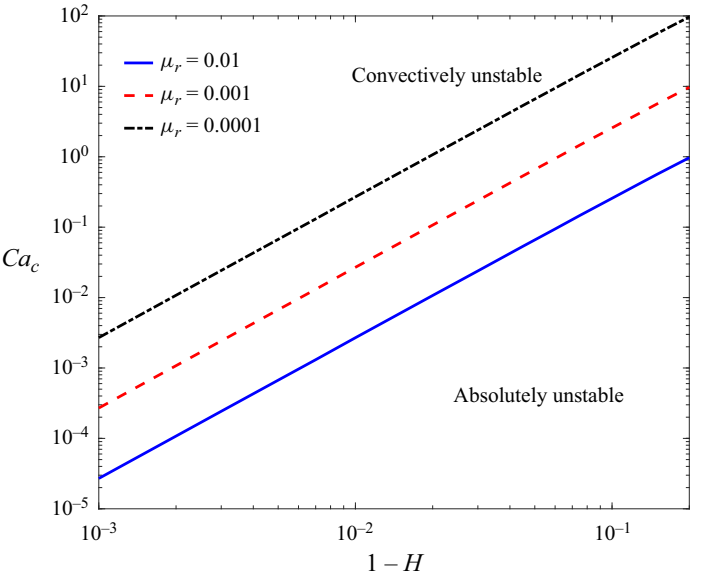


Figure 8. The variation of the critical capillary number Ca_c with the dimensionless thickness of the ASL layer $1 - H$ for $Re = 0$, $n = 1$ and $W = 0$. The curves exhibit scaling $Ca_c \sim (1 - H)^2$.

For a healthy lung, in the higher-generation airways, the thickness of the ASL layer is $\sim O(10^{-6} - 10^{-7})$ m while the airway lumen radius is $\sim O(10^{-3} - 10^{-4})$ m; thus $H \sim 0.999$ (Widdicombe & Widdicombe 1995; Widdicombe 1997; Moriarty & Grotberg 1999; Montaudon *et al.* 2007; Furlow & Mathisen 2018; Karamaoun *et al.* 2018). This corresponds to $1 - H = 0.001$ in figure 8. For $H \sim 0.999$, the calculations show that the flow is absolutely unstable provided that $Ca < 0.00027$. To achieve such a low $Ca = \mu_s V_c / \Sigma$, the velocity of the air (V_c) must drop significantly since the ASL viscosity and air–ASL interfacial tension are constant. Such a severe drop in V_c could occur towards the end of expiration in the breathing cycle (Pedley 1977). Thus, even in a healthy lung, absolute instability can exist, which could lead to airway closure in the airways during the end phase of the expiration in agreement with the previous studies (Burger & Macklem 1968; Heil *et al.* 2008). These liquid blockages normally rupture in the beginning phase of inspiration. As inspiration begins, the Ca value will increase and flow once again becomes convectively unstable, thereby prohibiting the airway closure.

In a lung suffering from diseases (e.g. cystic fibrosis and pulmonary oedema), there could be an increase in the thickness and viscosity of the ASL mainly due to the alteration in the properties and increasing thickness of the mucus layer (Hwang *et al.* 1969; Shah *et al.* 1996; Heil *et al.* 2008; Lai *et al.* 2009; Chen *et al.* 2019). Previous studies have indicated a higher chance of airway closure in diseased lungs (Heil *et al.* 2008; Halpern *et al.* 2010; Erken *et al.* 2023). An increase in the ASL thickness and viscosity leads to the exacerbation of the absolute instability in two ways. An increasing ASL thickness implies a high value of $1 - H$. From figure 8, as the ASL thickness increases, larger values of Ca become accessible for the flow to exhibit absolute instability. Simultaneously, an increasing viscosity of the ASL implies a decreasing μ_r. From figure 8, a decreasing μ_r shifts the absolute instability boundary to higher Ca. Thus, flow can exhibit absolute instability even at a higher Ca. To conclude, a pulmonary disease affecting the ASL layer enhances the possibility of an absolutely unstable flow in the higher-generation

https://doi.org/10.1017/jfm.2024.1116 Published online by Cambridge University Press

airways, thereby increasing the possibility of airway closure, in excellent agreement with the experimental and clinical observations (Mall 2016).

Also, from figure 8, if one were to plot $\mu_r Ca_c$ instead of Ca_c, then the three curves would overlap, indicating the scaling $Ca_c \sim 1/\mu_r$. Thus, the critical capillary number for the flow to become convectively unstable scales with the dimensionless thickness of the ASL and viscosity ratio as $Ca_c \sim (1-H)^2/\mu_r$.

7.2. *Effect of inertia (Re)*

Due to considerable air velocity in a certain generation of airways (Pedley 1977), there are appreciable inertial effects, as indicated by high values of Re in table 1. Thus, in this section, we analyse the effect of a finite Re on the existence of absolute instability. From figure 7(*c*), the flow is convectively unstable for $Ca = 1$ for $Re = 0$. If we increase Re to 100 while keeping other parameters the same as in figure 7(*c*), then the cusp point changes to $\omega_0 = 0.0001172 + 9.821 \times 10^{-6} i$, thus there is an absolutely unstable flow. This indicates the supporting role of the inertial effects in introducing absolute instability.

To further explore the effect of inertia, the variation of Ca_c with $1-H$ is shown in figure 9 for $Re = 100$. The inertial effects curtail the convectively unstable region for a higher thickness of the ASL. The airway cross-sectional area becomes narrower for a diseased lung with a high ASL layer thickness. Now, to maintain the appropriate gas exchange balance, the same volume of gas must flow through a lesser cross-section. This can result in an increase in the air velocity associated with rapid breathing. This increases the inertial effects in the airways since $Re = \rho_2 V_c R/\mu_s$ and increase in the capillary number since $Ca = \mu_s V_c/\Sigma$. From figure 9, if the capillary number increases faster than the Reynolds number and the ASL thickness is not appreciable, then the flow could become convectively unstable, thereby avoiding airway closure due to absolute instability. However, once the thickness of the ASL crosses a threshold value, the effect of the increased inertia comes into play, and the flow becomes absolutely unstable for an arbitrarily high value of Ca, thus leading to airway closure.

For a healthy lung, during exercise, an increased air velocity due to rapid breathing will increase Re and Ca. However, this will decrease the airway closure possibility due to an increase in Ca_c since the thickness $1-H \sim 0.001$ for which the inertial effects do not affect the absolute instability (see figure 9). To conclude, increasing air velocity could increase the risk of airway closure due to inertial effects in diseased lungs while having the opposite effect on healthy lungs.

7.3. *Effect of shear thinning (n)*

The ASL exhibits a strong shear thinning with power-law index $n \sim 0.1$–0.5 (Lai *et al.* 2009). In this section, we will analyse the effect of ASL shear thinning on the absolute instability parametric regions. To obtain a flavour of the modifications brought about by the shear thinning, consider a parameter set $Ca = 10$, $H = 0.95$, $\mu_r = 0.001$, $Re = 0$, $W = 0$ and $n = 1$ for which the cusp point is $\omega_0 = 0.000101166 - 0.0000127818i$. Now, if we introduce shear thinning by varying $n = 0.3$, the cusp point shifts to $\omega_0 = 0.000113344 + 0.0000272691i$. Thus, the shear thinning increases the threshold Ca at which the flow becomes convectively unstable. The effect of the power-law index on the absolute instability region is shown in figure 10. The shear thinning enables a higher Ca range accessible for the absolute instability. Note that pulmonary diseases (e.g. cystic fibrosis) can exacerbate the shear-thinning nature of the ASL owing to the increased concentration of the mucins in the mucus. Thus, in addition to the increased viscosity

https://doi.org/10.1017/jfm.2024.1116 Published online by Cambridge University Press

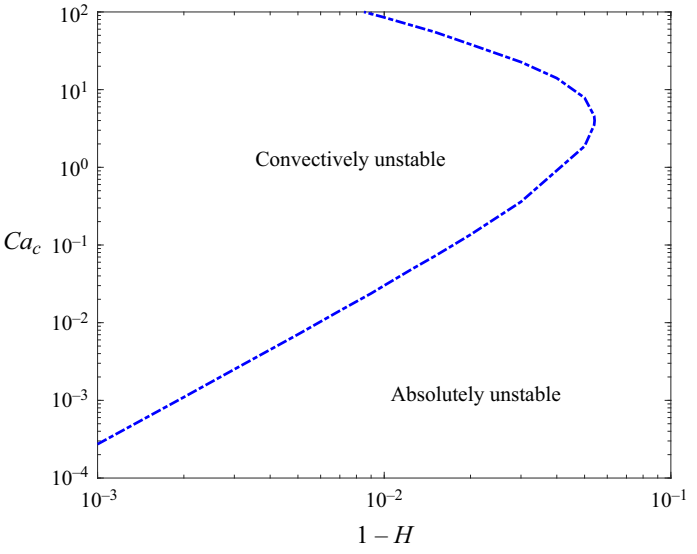


Figure 9. The variation of the critical capillary number (Ca_c) with the dimensionless thickness of the ASL ($1-H$) for $Re = 100$, $W = 0$, $\mu_r = 0.001$, $n = 1$ and $\rho_r = 0.001$. From the location of the turning point of the curve, the flow is absolutely unstable for arbitrarily high Ca for $1-H > 0.054$ or $H < 0.946$.

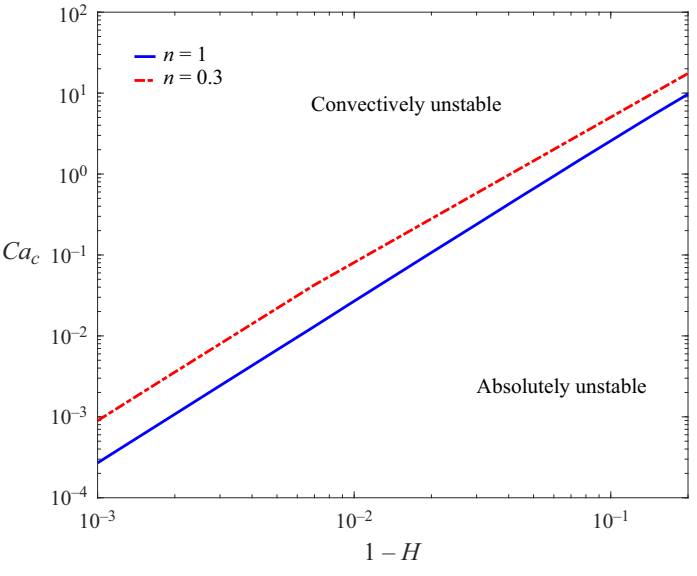


Figure 10. The variation of the critical capillary number Ca_c with the dimensionless thickness of the ASL layer $1-H$ for $Re = 0$, $\mu_r = 0.001$ and $W = 0$. The figure shows that ASL shear thinning enlarges the absolutely unstable region.

and thickness, pulmonary diseases increase the probability of absolute instability induced airway closure through enhanced shear thinning.

https://doi.org/10.1017/jfm.2024.1116 Published online by Cambridge University Press

W	ω_0
0	$0.00008940 + 0.0001241i$
10	$0.00008941 + 0.0001242i$
100	$0.00008951 + 0.0001247i$

Table 3. The location of the cusp point (ω_0) for select values of the Weissenberg number (W). The other parameters are $Ca = 0.1$, $Re = 0$, $\mu_r = 0.001$, $n = 1$ and $H = 0.95$. The table demonstrates the weak effect of the variation in ASL elasticity on absolute instability.

7.4. *Effect of elasticity (W)*

The mucus layer in the ASL exhibits strong viscoelastic properties (Lai *et al.* 2009; Hill *et al.* 2014). Thus, in this section, we explore the effect of variation in the ASL elasticity (i.e. W) on the absolute instability. Table 3 shows the variation in the cusp point location due to variation in the Weissenberg number W. Even as W changes by two orders, there is a negligible change in the ω_{i0} value, indicating a negligible effect of the ASL elasticity on the absolute instability in the higher-generation airways. Note that a pulmonary disease also increases ASL elasticity along with the viscosity and thickness (Lai *et al.* 2009; Hill *et al.* 2014). An increasing ASL elasticity does not majorly affect the absolute instability, while from § 7.1, increasing ASL viscosity and thickness have a strong effect on the existence of absolute instability. Additionally, for $n < 1$, the elastic mode exhibits a further decrease in the growth rate for the parameters relevant to the higher-generation airways, implying a decreasing role of the elastic mode in introducing absolute instability. Thus, pulmonary diseases primarily affect airway closure probability through the increase in the viscosity, shear thinning and thickness of the ASL.

8. Summary

In the present study, we analyse the temporal and spatio-temporal stability of flow in the higher-generation airways. Unlike turbulent airflow in the proximal or lower-generation airways, the airflow in the higher-generation airways is laminar. Thus, we treat this as a core–annular flow with air as the core fluid and ASL as the annular fluid. Owing to the shear-thinning viscoelastic properties of the ASL, we utilise the WM model for the annular fluid while the core fluid is treated as a Newtonian fluid. Additionally, we consider density and viscosity stratified flow due to the large difference in the densities and viscosities of the air and ASL.

The general linear temporal stability analysis predicts three unstable long-wave modes, in agreement with the previous studies. First, the Yih mode arises due to the viscosity stratification. Second, the elastic mode is due to the first normal stress difference across the air–ASL interface. Third, the capillary mode is due to the air–ASL interfacial tension. The temporal stability analysis reveals that, for the parameters relevant to the higher-generation airways, the three modes mentioned above will contribute to the destabilisation of the ASL. The shear thinning destabilises the capillary mode and stabilises the elastic mode.

The experiments of Guillot *et al.* (2007, 2008) and Utada *et al.* (2007) on core–annular flows showed the existence of a continuous core-fluid jet, core-fluid drops and annular liquid slug formation depending on the flow parameters. A lubrication-theory-based model of Guillot *et al.* (2007) concluded that the formation of the core-fluid drops and annular liquid slug is a consequence of an absolute instability. Thus, if the flow in the

https://doi.org/10.1017/jfm.2024.1116 Published online by Cambridge University Press

higher-generation airways exhibits absolute instability, then it could lead to the formation of air bubbles and ASL slugs. The presence of air bubbles or ASL slugs implies the presence of liquid bridges similar to those originating from the film collapse described in Heil *et al.* (2008), or ASL plugs predicted by Romano *et al.* (2019) that are responsible for airway closure. Thus, an absolutely unstable flow, if it exists in the higher-generation airways, may lead to airway closure. However, the existence of an absolutely unstable flow in these airways cannot be immediately concluded from the previous studies due to the extreme parametric range relevant to the higher-generation airways that remains unexplored in the previous analyses due to extreme density and viscosity stratification, the effect of inertial forces and the shear-thinning viscoelastic nature of the ASL. The present study is aimed at addressing this important missing gap.

In the spirit of the lubrication-theory-based model of Guillot *et al.* (2007) and long-wave equation of Camassa *et al.* (2014) owing to the long-wave nature of the unstable modes, here, we derive an evolution equation for the long-wave perturbations and analyse the temporal and spatio-temporal stability using the resulting dispersion relation. To probe for absolute instability, we utilise a combination of the analytical calculations and the Kupfer *et al.* (1987) method.

The present analysis reveals the possibility of an absolutely unstable flow in the higher-generation airways in certain parametric regimes. This leads to the existence of the critical capillary number Ca_c such that, for $Ca < Ca_c$, the flow will be absolutely unstable for vanishing Reynolds number Re. The parameter Ca_c exhibits the scaling of $Ca_c \sim (1-H)^2/\mu_r$, where $1-H$ is the dimensionless thickness of the ASL, and μ_r is the ratio of the air viscosity to the ASL viscosity.

In agreement with the clinical observations of Burger & Macklem (1968) and suggestions of Heil *et al.* (2008), for a healthy lung, where the ASL thickness is $H \sim 0.999$, our analysis predicts absolute instability only at the end of expiration during a breathing cycle owing to the drop in Ca value triggered by the low air velocity. In diseased lungs, the ASL thickness and viscosity can drastically increase. From the scaling $Ca_c \sim (1-H)^2/\mu_r$, one can immediately conclude that this will enhance the possibility of absolutely unstable flow and thus airway closure, in agreement with the experimental studies (Mall 2016).

Due to the substantial air velocity in the earlier generations of the distal airways, we also analyse the effect of the Reynolds number on the absolute instability. An increasing Re curtails the convectively unstable region in $(1-H)-Ca_c$ parametric space, thereby increasing the possibility of airway closure. A patient with a diseased lung can exhibit a higher Re due to rapid breathing. This could further enhance the occurrence of airway closure. Due to the small thickness of the ASL in healthy lungs, an increasing air velocity (e.g. due to exercise) reduces the airway closure probability. The ASL also exhibits a strong shear thinning with the power-law index $n \sim 0.1$–0.5. The analysis shows that an increasing shear thinning leads to a bigger absolute instability region, thereby enhancing the probability of airway closure. The ASL elasticity has a negligible effect on the absolute instability.

The above conclusions must be considered in light of the following shortcomings of the present study. Due to breathing, an oscillatory flow exists in the airways, which could modify the occurrence of absolute instability. Additionally, repeated airway bifurcation can affect the convective to absolute transition. These factors have been neglected in the flow model considered here in order to simplify the complicated flow conditions and make the flow amenable to theoretical treatment. The present study could be extended by considering these modifications. Also, in the present analysis, the instability has not

https://doi.org/10.1017/jfm.2024.1116 Published online by Cambridge University Press

been tracked until the airway closure by considering the nonlinear development of the perturbations. Rather, the conclusions of the present study are based on the experimental outcomes of Guillot *et al.* (2007). We have treated the ASL as a single layer by considering the average properties of the mucus and serous layers. One could extend the present study by considering a three-layer flow of air, mucus and serous layers. Careful experiments could validate the predictions of the present analysis.

Acknowledgements. The author acknowledges financial support from the Indian Institute of Technology Hyderabad, India, under grant SG/IITH/F280/2022-23/SG-118 and SERB-DST under grant SRG/2023/000223.

Declaration of interests. The author reports no conflict of interest.

Author ORCID.
Ramkarn Patne https://orcid.org/0000-0003-4052-1807.

References

Abrahams, I.D., Davis, A.M.J. & Smith, S.G.L. 2008 Asymmetric channel divider in stokes flow. *SIAM J. Appl. Math.* **68**, 1439–1463.

Badr, H., Dennis, S.C.R., Bates, S. & Smith, F.T. 1985 Numerical and asymptotic solutions for merging flow through a channel with an upstream splitter plate. *J. Fluid Mech.* **156**, 63–81.

Bassom, A.P., Blyth, M.G. & Papageorgiou, G.T. 2012 Using surfactants to stabilize two-phase pipe flows of core-annular type. *J. Fluid Mech.* **704**, 333–359.

Briggs, R.J. 1964 *Electron-stream Interaction with Plasmas*. MIT Press.

Burger, E.J. & Macklem, P. 1968 Airway closure: demonstration breathing 100 % O_2 at low lung volumes and by N_2 washout. *J. Appl. Physiol.* **25**, 139–148.

Camassa, R., Ogrosky, H.R. & Olander, J. 2014 Viscous film flow coating the interior of a vertical tube. Part 1. Gravity-driven flow. *J. Fluid Mech.* **745**, 682–715.

Camassa, R., Ogrosky, H.R. & Olander, J. 2017 Viscous film-flow coating the interior of a vertical tube. Part 2. Air-driven flow. *J. Fluid Mech.* **825**, 1056–1090.

Castillo, H.A. & Wilson, H.J. 2017 Towards a mechanism for instability in channel flow of highly shear-thinning viscoelastic fluids. *J. Non-Newtonian Fluid Mech.* **247**, 15–21.

Chen, K.P. 1991 Interfacial instability due to elastic stratification in concentric coextrusion of two viscoelastic fluids. *J. Non-Newtonian Fluid Mech.* **40**, 155–175.

Chen, Z., Zhong, M., Luo, Y., Deng, L., Hu, Z. & Song, Y. 2019 Determination of rheology and surface tension of airway surface liquid: a review of clinical relevance and measurement techniques. *Respir. Res.* **20**, 274.

Crystal, R. 1997 *The Lung: Scientific Foundations*. Wiley.

Dietze, G.F. 2022 *Falling Liquid Films in Narrow Geometries and Other Thin Film Flows*. Fluids Mechanics. Universite Paris-Saclay.

Dietze, G.F., Lavalle, G. & Ruyer-Quil, C. 2020 Films in narrow tubes: occlusion scenarios. *J. Fluid Mech.* **894**, A17.

Dietze, G.F. & Ruyer-Quil, C. 2015 Films in narrow tubes. *J. Fluid Mech.* **762**, 68–109.

Erken, O., Fazla, B., Muradoglu, M., Izbassarov, D., Romanò, F. & Grotberg, J.B. 2023 Effects of elastoviscoplastic properties of mucus on airway closure in healthy and pathological conditions. *Phys. Rev. Fluids* **8**, 053102.

Erken, O., Romano, F., Grotberg, J.B. & Muradoglu, M. 2021 Capillary instability of a two-layer annular film: an airway closure model. *J. Fluid Mech.* **934**, A7.

Furlow, P.W. & Mathisen, D.J. 2018 Surgical anatomy of the trachea. *Ann. Cardiothorac. Surg.* **7** (2), 255–260.

Gaurav, & Shankar, V. 2007 Stability of gravity-driven free-surface flow past a deformable solid layer at zero and finite Reynolds number. *Phys. Fluids* **19**, 024105.

Gaurav, & Shankar, V. 2013 Manipulation of instabilities in core-annular flows using a deformable solid layer. *Phys. Fluids* **25**, 014104.

Govindarajan, R. & Sahu, K.C. 2014 Instabilities in viscosity-stratified flows. *Annu. Rev. Fluid Mech.* **46**, 331–353.

Grotberg, J.B. 2011 Respiratory fluid mechanics. *Phys. Fluids* **23** (2), 021301.

https://doi.org/10.1017/jfm.2024.1116 Published online by Cambridge University Press

GROTBERG, J.B. & JENSEN, O.E. 2004 Biofluid mechanics in flexible tubes. *Annu. Rev. Fluid Mech.* **36**, 121–147.

GUILLOT, P., COLIN, A. & AJDARI, A. 2008 Stability of a jet in confined pressure-driven biphasic flows at low Reynolds number in various geometries. *Phys. Rev.* E **78**, 016307.

GUILLOT, P., COLIN, A., UTADA, A.S. & AJDARI, A. 2007 Stability of a jet in confined pressure-driven biphasic flows at low Reynolds numbers. *Phys. Rev. Lett.* **99**, 104502.

HALPERN, D., FUJIOKA, H. & GROTBERG, J.B. 2010 The effect of viscoelasticity on the stability of a pulmonary airway liquid layer. *Phys. Fluids* **22**, 011901.

HALPERN, D & GROTBERG, J.B. 1992 Fluid-elastic instabilities of liquid-lined flexible tubes. *J. Fluid Mech.* **244**, 615–632.

HALPERN, D. & GROTBERG, J.B. 1993 Surfactant effects on fluid-elastic instabilitiies of liquid-lined flexible tubes: a model of airway closure. *Trans. ASME J. Biomech. Engng* **115**, 271–277.

HAMED, R. & FIEGEL, J. 2014 Synthetic tracheal mucus with native rheological and surface tension properties. *J. Biomed. Mater. Res.* A **102** (6), 1788–1798.

HEIL, M., HAZEL, A.L. & SMITH, J.A. 2008 The mechanics of airway closure. *Respir. Physiol. Neurobiol.* **163**, 214–21.

HILL, D.B., *et al.* 2014 A biophysical basis for mucus solids concentration as a candidate biomarker for airways disease. *PLoS One* **138**, e87681.

HU, H.H. & PATANKAR, N. 1995 Non-axisymmetric stability of core-anular flow. *J. Fluid Mech.* **290**, 213–224.

HUERRE, P. & MONKEWITZ, P.A. 1990 Local and global instabilities in spatially developing flows. *Annu. Rev. Fluid Mech.* **22**, 173–537.

HWANG, S.H., LITT, M. & FORSMAN, W.C. 1969 Rheological properties of mucus. *Rheol. Acta* **8**, 438–448.

INCROPERA, F.P., DEWITT, D.P., BERGMAN, T.L. & LAVINE, A.S. 2007 *Fundamentals of Heat and Mass Transfer*. Wiley.

JAIN, M. & SZNAJDER, J.I. 2007 Bench to bed-side review: distal airways in acute respiratory distress syndrome. *Crit. Care* **11**, 206.

JOSEPH, D.D., BAI, R., CHEN, K.P. & RENARDY, Y.Y. 1997 Core-annular flows. *Annu. Rev. Fluid Mech.* **29**, 65–90.

KARAMAOUN, C., SOBAC, B., MAUROY, B., VAN MUYLEM, A. & HAUT, B. 2018 New insights into the mechanisms controlling the bronchial mucus balance. *PLos One* **13**, e0199319.

KLEINSTREUER, C. & ZHANG, Z. 2009 An adjustable triple-bifurcation unit (TBU) model for air-particle flow simulations in human tracheobronchial airways. *Trans. ASME J. Biomech. Engng* **131**, 021007.

KLEINSTREUER, C. & ZHANG, Z. 2010 Air flow and particle transport in the human respiratory system. *Annu. Rev. Fluid Mech.* **42**, 301–34.

KUPFER, K., BERS, A. & RAM, A.K. 1987 The cusp map in complex-frequency plane for absolute instabilities. *Phys. Fluids* **30**, 10.

LAFFORGUE, O., SEYSSIECQ-GUARANTE, I., PONCET, S. & FAVIER, J. 2017 Rheological properties of synthetic mucus for airway clearance. *J. Biomed. Mater. Res.* A **106**, 386.

LAI, S.K., WANG, Y.Y., WIRTZ, D. & HANES, J. 2009 Micro- and macrorheology of mucus: implications for drug and gene delivery to mucosal tissues. *Adv. Drug Deliv. Rev.* **61**, 86–100.

LI, M., XU, S. & KUMACHEVA, E. 2000 Convection in polymeric fluids subjected to vertical temperature gradients. *Macromolecules* **33**, 4972–4978.

LIN, C.L., TAWHAI, M.H., MCLENNAN, G. & HOFFMAN, E.A. 2007 Characteristics of the turbulent laryngeal jet and its effect on airflow in the human intrathoracic airways. *Respir. Physiol. Neurobiol.* **157**, 295–309.

MALL, M.A. 2016 Unplugging mucus in cystic fibrosis and chronic obstructive pulmonary disease. *Ann. Am. Thorac. Soc.* **13**, S177–S185.

MONTAUDON, M., DESBARATS, P., BERGER, P., DE DIETRICH, G., MARTHAN, R. & LAURENT, F. 2007 Assessment of bronchial wall thickness and lumen diameter in human adults using multi-detector computed tomography: comparison with theoretical models. *J. Anat.* **211** (5), 579–588.

MORIARTY, J.A. & GROTBERG, J.B. 1999 Flow-induced instabilities of a mucus-serous bilayer. *J. Fluid Mech.* **397**, 1–22.

MURADOGLU, M., ROMANO, F., FUJIOKA, H. & GROTBERG, J.B. 2021 Effects of surfactant on propagation and rupture of a liquid plug in a tube. *J. Fluid Mech.* **872**, 407.

ORON, A., DAVIS, S.H. & BANKOFF, S.G. 1997 Long-scale evolution of thin liquid films. *Rev. Mod. Phys.* **69**, 931–980.

PATNE, R. 2021 Purely elastic instabilities in the airways and oral area. *J. Fluid Mech.* **928**, A22.

https://doi.org/10.1017/jfm.2024.1116 Published online by Cambridge University Press

PATNE, R. 2024 Effect of inhaled air temperature on mucus layer in the proximal airways. *J. Fluid Mech.* **978**, A15.

PATNE, R., AGNON, Y. & ORON, A. 2021 Thermocapillary instabilities in a liquid layer subjected to an oblique temperature gradient. *J. Fluid Mech.* **906**, A12.

PATNE, R. & CHANDARANA, J. 2023 Spatio-temporal dynamics of a two-layer pressure-driven flow subjected to a wall-normal temperature gradient. *J. Fluid Mech.* **957**, A11.

PATNE, R., MANDLOI, S., SHANKAR, V. & SUBRAMANIAN, G. 2024 Instabilities in strongly shear-thinning viscoelastic flows through channels and tubes. arXiv:2408.01004

PATNE, R. & RAMON, G.Z. 2020 Stability of fluid flows coupled by a deformable solid layer. *J. Fluid Mech.* **905**, A36.

PATNE, R. & SHANKAR, V. 2017 Absolute and convective instability in combined Couette–Poiseuille flow past a neo-Hookean solid. *Phys. Fluids* **29**, 124104.

PATNE, R. & SHANKAR, V. 2020 Instability induced by wall deformability in sliding Couette flow. *Phys. Fluids* **32**, 114102.

PEDLEY, T.J. 1977 Pulmonary fluid dynamics. *Annu. Rev. Fluid Mech.* **9**, 229–274.

ROMANO, F., FUJIOKA, H., MURADOGLU, M. & GROTBERG, J.B. 2019 Liquid plug formation in an airway closure model. *Phys. Rev. Fluids* **4** (9), 093103.

ROMANO, F., MURADOGLU, M., FUJIOKA, H. & GROTBERG, J.B. 2021 The effect of viscoelasticity in an airway closure model. *J. Fluid Mech.* **913**, 1–26.

ROMANO, F., MURADOGLU, M. & GROTBERG, J.B. 2022 Effect of surfactant in an airway closure model. *Phys. Rev. Fluids* **7**, 093103.

SAHU, K.C. 2021 A new linearly unstable mode in the core-annular flow of two immiscible fluids. *J. Fluid Mech.* **918**, A11.

SALIN, D. & TALON, L. 2019 Revisiting the linear stability analysis and absolute-convective transition of two fluid core annular flow. *J. Fluid Mech.* **865**, 743–761.

SAMANTA, A. 2013 Effect of surfactant on two-layer channel flow. *J. Fluid Mech.* **735**, 519–552.

SCHATZ, M.F. & NEITZEL, G.P. 2001 Experiments on thermocapillary instabilities. *Annu. Rev. Fluid Mech.* **33**, 93–127.

SCHMID, P.J. & HENNINGSON, D.S. 2001 *Stability and Transition in Shear Flows*. Springer.

SHAH, P.L., SCOTT, S.F., KNIGHT, R.A., MARRIOTT, C., RANASINHA, C. & HODSON, M.E. 1996 In vivo effects of recombinant human DNase I on sputum in patients with cystic fibrosis. *Thorax* **51**, 119–125.

SHEMILT, J.D., HORSLEY, A., JENSEN, O.E., THOMPSON, A.B. & WHITFIELD, C.A. 2022 Surface-tension-driven evolution of a viscoplastic liquid coating the interior of a cylindrical tube. *J. Fluid Mech.* **944**, A22.

SHEMILT, J.D., HORSLEY, A., JENSEN, O.E., THOMPSON, A.B. & WHITFIELD, C.A. 2023 Surfactant amplifies yield-stress effects in the capillary instability of a film coating a tube. *J. Fluid Mech.* **971**, A24.

STANDRING, S. 2016 *Gray's Anatomy: The Anatomical Basis of Clinical Practice*. Elsevier.

STOCKER, J.R. & DUCK, P.W. 1995 Stationary perturbations of Couette–Poiseuille flow: the flow development in long cavities and channels. *J. Fluid Mech.* **292**, 153–182.

TREFETHEN, L.N. 2000 *Spectral Methods in MATLAB*. SIAM.

UTADA, A.S., FERNANDEZ-NIEVES, A., GORDILLO, J.M. & WEITZ, D.A. 2008 Absolute instability of a liquid jet in a coflowing stream. *Phys. Rev. Lett.* **100**, 014502.

UTADA, A.S., FERNANDEZ-NIEVES, A., STONE, H.A. & WEITZ, D.A. 2007 Dripping to jetting transitions in coflowing liquid streams. *Phys. Rev. Lett.* **99**, 094502.

WEI, H.-H. 2005*a* Marangoni destabilization on a core-annular film flow due to the presence of a surfactant. *Phys. Fluids* **17**, 027101.

WEI, H.H. 2005*b* Thermocapillary instability of core-annular flows. *Phys. Fluids* **17**, 102102.

WEI, H.-H. & RUMSCHITZKI, D.S. 2005 The effect of insoluble surfactants on the linear stability of a core-annular flow. *J. Fluid Mech.* **541**, 115–142.

WEIBEL, E.R. & GOMEZ, D.M. 1962 Architecture of the human lung. *Science* **137**, 577.

WHITE, F.M. 2003 *Viscous Fluid Flow*. McGraw-Hill.

WHITE, J. & HEIL, M. 2005 Three-dimensional instabilities of liquid-lined elastic tubes: a thin-film fluid-structure interaction model. *Phys. Fluids* **17**, 031506.

WHITE, J.L. & METZNER, A.B. 1963 Development of constitutive equations for polymeric melts and solutions. *J. Appl. Polym. Sci.* **7**, 1867–1889.

WIDDICOMBE, J. 1997 Airway and alveolar permeability and surface liquid thickness: theory. *J. Appl. Physiol.* **82** (1), 3–12.

WIDDICOMBE, J.H. & WIDDICOMBE, J.G. 1995 Regulation of human airway surface liquid. *Respir. Physiol.* **99** (1), 3–12.

https://doi.org/10.1017/jfm.2024.1116 Published online by Cambridge University Press

WILSON, H.J. & LORIDAN, V. 2015 Linear instability of a highly shear-thinning fluid in channel flow. *J. Non-Newtonian Fluid Mech.* **223**, 200–208.

WILSON, H.J. & RALLISON, J.M. 1999 Instability of channel flow of a shear-thinning White-Metzner fluid. *J. Non-Newtonian Fluid Mech.* **87**, 75–96.

WILSON, H.J., RENARDY, M. & RENARDY, Y. 1999 Structure of the spectrum in zero Reynolds number shear flow of the UCM and Oldroyd-B liquids. *J. Non-Newtonian Fluid Mech.* **80**, 251–268.

XIA, G., TAWHAI, M.H., HOFFMAN, E.A. & LIN, C.-L. 2010 Airway wall stiffening increases peak wall shear stress: a fluid–structure interaction study in rigid and compliant airways. *Ann. Biomed. Engng* **38** (5), 1836–1853.

YEO, K.S., KHOO, B.C. & ZHAO, H.Z. 1999 The convective and absolute instability of fluid flow over viscoelastic compliant layers. *J. Sound Vib.* **223** (3), 379–398.

YEO, K.S., KHOO, B.C. & ZHAO, H.Z. 2001 Turbulent boundary layer over a compliant surface: absolute and convective instabilities. *J. Fluid Mech.* **449**, 141–168.

YIH, C.-S. 1967 Instability due to viscosity stratification. *J. Fluid Mech.* **27**, 337–350.

ZHOU, Z.-Q., PENG, J., ZHANG, Y.-J. & ZHUGE, W.-L. 2014 Instabilities of viscoelastic liquid film coating tube in the presence of surfactant. *J. Non-Newtonian Fluid Mech.* **204**, 94–103.

https://doi.org/10.1017/jfm.2024.1116 Published online by Cambridge University Press